

Theory of quantum-geometric charge and spin Josephson diode effects in strongly spin-polarized hybrid structures with noncoplanar spin textures

Niklas L. Schulz,^{1,*} Danilo Nikolić,^{1,†} and Matthias Eschrig^{1,‡}

¹*Institute of Physics, University of Greifswald, Felix-Hausdorff-Strasse 6, 17489 Greifswald, Germany*

(Dated: January 22, 2025)

We present a systematic study of the spin-resolved Josephson diode effect (JDE) in strongly spin-polarized ferromagnets (sFM) coupled to singlet superconductors (SC) via ferromagnetic insulating interfaces (FI). All metallic parts are described in the framework of the quasiclassical Usadel Green's function theory applicable to diffusive systems. The interfaces are characterized by an S-matrix obtained for a model potential with exchange vectors pointing in an arbitrary direction with respect to the magnetization in the sFM. Our theory predicts a large charge Josephson diode effect with an efficiency exceeding 33% and a perfect spin diode effect with 100% efficiency. To achieve these the following conditions are necessary: (i) a noncoplanar profile of the three magnetization vectors in the system and (ii) different densities of states of spin- \uparrow and spin- \downarrow bands in the sFM achieved by a strong spin polarization. The former gives rise to the quantum-geometric phase, $\Delta\varphi$, that enters the theory in a very similar manner as the superconducting phase difference across the junction, $\Delta\chi$. We perform a harmonic analysis of the Josephson current in both variables and find symmetries between Fourier coefficients allowing an interpretation in terms of transfer processes of multiple equal-spin Cooper pairs across the two ferromagnetic spin bands. We point out the importance of crossed pair transmission processes. Finally, we study a spin-switching effect of an equal-spin supercurrent by reversing the magnetic flux in a SQUID device incorporating the mentioned junction and propose a way for measuring it.

I. INTRODUCTION

Superconducting spintronics has the potential for new functionalities of spintronics devices based on equal-spin supercurrents [1–9]. Especially promising are devices involving strongly spin-polarized itinerant ferromagnets in a Josephson junction between two spin-singlet superconductors, in which phase-coherence in the ferromagnet is maintained only within each spin band, however not between the two spin bands [4, 10–18]. In superconductors with a conventional order parameter, Cooper pairs can be classified into singlet and triplet pairs. When penetrating a ferromagnet due to the superconducting proximity effect, the triplet Cooper pairs become inequivalent and divide into short-range and long-range pairs [19]. With respect to the ferromagnet's spin quantization axis, equal-spin $\uparrow\uparrow$ - and $\downarrow\downarrow$ -pair amplitudes are long-ranged in their respective spin band, whereas the third spin-triplet pair amplitude is short-ranged, just like the singlet amplitude, due to the decoherence induced by the exchange splitting of the electronic spin bands. Thus, the building blocks for superconducting spintronics are not the electron spins as in spintronics, but the spins of equal-spin Cooper pairs.

The creation and control of equal-spin Cooper pairs is based on two fundamental processes taking place near the interface of a superconductor and a ferromagnet: [20] (i) spin-mixing (or spin-dependent phase shifts)

and (ii) triplet rotation. The first process turns spin-singlet pairs into spin-triplet pairs, and the second process turns short-range amplitudes into long-range amplitudes. Whereas the first process merely requires a spin-polarization of the interface region, the second process requires a noncollinear spin arrangement. Spin-triplet supercurrents based on these mechanisms have been experimentally realized [21–28], and at present can be produced routinely.

Whereas long-range triplet supercurrents are a prerequisite of superconducting spintronics, important new functionalities appear when the spin-texture in the ferromagnet is not only noncollinear, but *noncoplanar*. Noncoplanar spin arrangements in strongly spin-polarized superconducting spintronics devices lead to an effective decoupling of the Josephson phases in the two spin bands and an opening of a new channel of control via *geometric phases* that directly add to the Josephson phases with opposite sign in the two spin bands [12]. We will show in the following that new phenomena occur in this case, that are entirely governed by quantum-geometric phases that appear due to noncoplanar spin textures in the device. Quantum-geometric phases play an important role in materials with nontrivial spin-structure like altermagnets [29–31], topological insulators [32–36], or skyrmionic materials [37–41]. In this article, we discuss the appearance of charge and spin Josephson-diode effects based on quantum-geometric phases, as well as a new channel of control for spin-polarized supercurrents, allowing for example for a switching between almost pure spin-up equal-spin supercurrents and spin-down equal-spin supercurrents.

From general considerations, it is well known that if the system is invariant under the time reversal and in-

* niklas.schulz@uni-greifswald.de

† danilo.nikolic@uni-greifswald.de

‡ matthias.eschrig@uni-greifswald.de

version operations, the normal Josephson effect, characterized by $I(-\Delta\chi) = -I(\Delta\chi) \implies I(\Delta\chi = 0) = 0$, appears [42]. However, if the mentioned symmetries are broken this relation can be violated and the so-called "ϕ₀-junction" may appear. This effect has been predicted in various setups including junctions with strong spin-orbit coupling [43], unconventional superconductors [44–46], or strongly spin-polarized itinerant ferromagnets [11, 12, 16], to mention a few. Furthermore, the presence of higher harmonics in the Josephson current-phase relation (CPR) leads to nonreciprocal transport. Namely, the critical current in one direction (+) can be different from that flowing in the opposite direction (−) leading to the so-called superconducting or Josephson diode effect (JDE) [47]. This effect has been intensively studied in numerous experimental [47–54] and theoretical works [12, 50, 55–76] in recent years. The figure of merit in this effect is the so-called diode efficiency defined as $\eta = (I^+ - |I^-|)/(I^+ + |I^-|)$ where I^\pm refers to the critical current in the corresponding direction. In the present work, we will focus on two effects of this kind: the charge and the spin Josephson diode effect showing that the former can reach efficiencies exceeding 33%, whereas the latter can reach an efficiency of up to 100%.

To illustrate the role of the noncoplanarity of the magnetization vectors in ferromagnetic trilayers, let us consider the spin rotation from one quantization axis (e.g. z -axis) to another one along a direction \mathbf{n} parameterized by the polar α and the azimuthal angle φ :

$$\begin{pmatrix} \uparrow \\ \downarrow \end{pmatrix}_{\mathbf{n}} = \begin{pmatrix} \cos \frac{\alpha}{2} & \sin \frac{\alpha}{2} e^{i\varphi} \\ -\sin \frac{\alpha}{2} e^{-i\varphi} & \cos \frac{\alpha}{2} \end{pmatrix} \begin{pmatrix} \uparrow \\ \downarrow \end{pmatrix}_z. \quad (1)$$

Consequently, the Cooper pair amplitudes transform as follows:

$$(\uparrow\downarrow - \downarrow\uparrow)_{\mathbf{n}} = (\uparrow\downarrow - \downarrow\uparrow)_z, \quad (2)$$

$$\begin{aligned} (\uparrow\uparrow + \downarrow\downarrow)_{\mathbf{n}} &= -\sin \alpha [e^{-i\varphi}(\uparrow\uparrow)_z - e^{i\varphi}(\downarrow\downarrow)_z] \\ &\quad + \cos \alpha (\uparrow\uparrow + \downarrow\downarrow)_z. \end{aligned} \quad (3)$$

We draw two important conclusions here. First, once a mixed-spin triplet Cooper pair [see Eq. (3)] is formed along the magnetic moment of the SC/sFM interface (set to be along the \mathbf{n} direction), it can give rise to equal-spin triplets along the magnetization in the sFM (set to be the z -direction). Second, the two equal-spin triplet amplitudes, $(\uparrow\uparrow)_z$ and $(\downarrow\downarrow)_z$, acquire a relative phase $\pm(2\varphi + \pi)$ with respect to each other. As we show below, the difference $\Delta\varphi$ of the phase shifts at the two SC/sFM interfaces of the Josephson junction corresponds to the *geometric phase difference* which in combination with ferromagnetic spin-filtering leads to the appearance of the Josephson diode effect. Moreover, we show that for a given magnetization profile there is a Josephson phase for which the supercurrent is nearly fully spin polarized. Considering a SQUID geometry which incorporates the discussed junction, we propose a device that can switch between spin-up and spin-down Josephson currents.

The paper is organized as follows. In Sec. II we provide general remarks on the quasiclassical Green's function method used for calculating the transport properties. In Sec. III we present a microscopic description of the system under study, consisting of a strong ferromagnet coupled to two BCS superconductors via ferromagnetic interfaces. In Sec. IV we discuss the boundary conditions which turn out to be crucial for the appearance of the quantum-geometric effects that leads to the Josephson diode effect. In Sec. V we present the results of our numerical calculations and analyze in detail the Josephson charge and spin diode effects. Finally, in Sec. VI we enclose the discussion by giving the concluding remarks.

II. QUASICLASSICAL THEORY

For the theoretical description, we make use of the quasiclassical theory of superconductivity of Eilenberger [77] and Larkin and Ovchinnikov [78] within the limit of diffusive systems, the Usadel theory [79–81]. This limit is realized in systems where the elastic mean free path $\ell = v_F\tau$ is much smaller than the superconducting coherence length of a ballistic superconductor $\sim \hbar v_F/\Delta_0$ with v_F being the Fermi velocity in the superconductor and Δ_0 the superconducting order parameter at $T = 0$. As our main objective is the description of junctions comprising strongly spin-polarized ferromagnets, $J \sim E_F$, the Usadel theory cannot be applied directly, but a modified description is required [12–14, 16–18].

In this work we focus on equilibrium properties of the system making the consideration of the retarded Green's function $\hat{G}^R(\mathbf{R}, E)$ sufficient. Since we only need this Green's function component, we will omit the R in the exponent in the following, denoting it only as $G(\mathbf{R}, E)$ and referring to it as the Green's function. Note that here $\mathbf{R} = (x, y, z)^T$ and E denote the spatial center-of-mass coordinate and the energy, respectively. The $\hat{\cdot}$ symbol denotes objects defined in combined particle-hole \otimes spin space spanned by the Gor'kov-Nambu bispinor $\Psi = (\psi_\uparrow, \psi_\downarrow, \psi_\uparrow^\dagger, \psi_\downarrow^\dagger)$. Consequently, the retarded Green's function is a 2×2 matrix in particle-hole space

$$\hat{G} = \begin{pmatrix} \mathcal{G} & \mathcal{F} \\ -\tilde{\mathcal{F}} & -\tilde{\mathcal{G}} \end{pmatrix}, \quad (4)$$

where each entry itself is a 2×2 matrix in spin space. Note that $\hat{\cdot}$ denotes a particle-hole symmetry relation $\tilde{Q}(\mathbf{R}, E) = Q(\mathbf{R}, -E^*)^*$ [82, 83]. The matrix structure in spin space can be further decomposed as [82]

$$\hat{G} = \begin{pmatrix} \mathcal{G}_0 1 + \mathcal{G} \cdot \boldsymbol{\sigma} & (\mathcal{F}_0 1 + \mathcal{F} \cdot \boldsymbol{\sigma}) i\sigma_y \\ -i\sigma_y (\tilde{\mathcal{F}}_0 1 + \tilde{\mathcal{F}} \cdot \boldsymbol{\sigma}) & -(\tilde{\mathcal{G}}_0 1 + \tilde{\mathcal{G}} \cdot \boldsymbol{\sigma}^*) \end{pmatrix} \quad (5)$$

where $\boldsymbol{\sigma} = (\sigma_x, \sigma_y, \sigma_z)^T$ is the Pauli vector in spin space, $1 = \text{diag}(1, 1)$ is the identity matrix in spin space, \mathcal{F}_0 and $\mathcal{F} = (\mathcal{F}_x, \mathcal{F}_y, \mathcal{F}_z)^T$ are the singlet and triplet pair amplitudes, respectively, and \mathcal{G}_0 and $\mathcal{G} = (\mathcal{G}_x, \mathcal{G}_y, \mathcal{G}_z)^T$ are the spin-scalar and spin-vector contributions to \mathcal{G} .

The Green's function is determined by solving the Usadel equation with normalization condition [79–81],

$$[E\hat{\tau}_3 - \hat{\Delta}, \hat{G}] - i\hbar \sum_{k,l} D_{kl} \nabla_k (\hat{G} \nabla_l \hat{G}) = \hat{0}, \quad \hat{G}^2 = \hat{1}, \quad (6)$$

where $\hat{\tau}_3 = \text{diag}(1, -1)$ is the third Pauli matrix in particle-hole \otimes spin space, $k, l \in \{x, y, z\}$, and the gap matrix $\hat{\Delta}$ for spin-singlet BCS pairing is given by

$$\hat{\Delta} = \begin{pmatrix} 0 & \Delta \\ \Delta^* & 0 \end{pmatrix}, \quad (7)$$

where the entries have a simple spin structure, $\Delta \propto i\sigma_y$. To obtain the full solution, the spatially varying superconducting gap should be calculated self-consistently

$$\Delta(\mathbf{R}) = \lim_{c \rightarrow \infty} \frac{-\int_{-c}^c \frac{dE}{2} \mathcal{F}_0(\mathbf{R}, E) \tanh \frac{E}{2k_B T}}{\ln \frac{T}{T_c} + \int_{-c}^c \frac{dE}{2E} \tanh \frac{E}{2k_B T}} i\sigma_y, \quad (8)$$

where T_c is the superconducting critical temperature. Finally, D_{kl} is the diffusion coefficient which is, in general, a tensor. However, for an isotropic Fermi surface and electron-impurity scattering as considered in this paper, it takes a simple form $D_{kl} = D\delta_{kl}$ where $D = v_F^2 \tau / 3$, with τ the impurity scattering time.

The Green's function formalism furthermore allows to express the expectation values of observables in a compact form. In this work, we mainly focus on the charge and spin currents in quasi-one-dimensional wires, which in terms of the Usadel Green's functions for spin-degenerate diffusion constants (D) and densities of states at the Fermi level (N_F) are given by, respectively,

$$I_{\text{charge}} = eN_F D \text{Re} \int_{-\infty}^{\infty} \frac{dE}{4} \text{Tr} \left[\hat{\tau}_3 \hat{G} \partial_z \hat{G} \right] \tanh \frac{E}{2k_B T}, \quad (9)$$

$$I_{\text{spin}} = \frac{\hbar}{2} N_F D \text{Re} \int_{-\infty}^{\infty} \frac{dE}{4} \text{Tr} \left[\hat{\tau}_3 \hat{\sigma} \hat{G} \partial_z \hat{G} \right] \tanh \frac{E}{2k_B T}. \quad (10)$$

Here, $e = -|e|$ is the electron charge, z is the spatial coordinate in positive current direction, $\hat{\sigma} = (\hat{\sigma}_x, \hat{\sigma}_y, \hat{\sigma}_z)^T$ with $\hat{\sigma}_i = \text{diag}(\sigma_i, \sigma_i)$ with $i = x, y, z$, and the trace is performed over the entire 4×4 particle-hole \otimes spin space.

A. Coherence functions

In the following, we consider spin-dependent phenomena arising in the vicinity of superconductor-ferromagnet interfaces and thereby we must maintain the full spin structure of the problem. To do so, we utilize the so-called Riccati parameterization [83–89], where the Green's function is expressed in terms of coherence (Riccati) functions γ and $\tilde{\gamma}$ as

$$\hat{G} = \hat{N} \begin{pmatrix} (1 + \gamma\tilde{\gamma}) & 2\gamma \\ -2\tilde{\gamma} & -(1 + \tilde{\gamma}\gamma) \end{pmatrix}, \quad (11)$$

with \hat{N} being the normalization matrix given by [83]

$$\hat{N} = \begin{pmatrix} (1 - \gamma\tilde{\gamma})^{-1} & 0 \\ 0 & (1 - \tilde{\gamma}\gamma)^{-1} \end{pmatrix} = \begin{pmatrix} N & 0 \\ 0 & \tilde{N} \end{pmatrix}. \quad (12)$$

In general, the coherence functions γ and $\tilde{\gamma}$ are 2×2 matrices in spin space obeying the following equations of motion [see Eq. (6)] [89–91]:

$$\frac{\partial^2 \gamma}{\partial z^2} + \frac{\partial \gamma}{\partial z} \tilde{\mathcal{F}} \frac{\partial \gamma}{\partial z} = \frac{i}{\hbar D} [\gamma \Delta^* \gamma - 2E\gamma - \Delta], \quad (13)$$

$$\frac{\partial^2 \tilde{\gamma}}{\partial z^2} + \frac{\partial \tilde{\gamma}}{\partial z} \mathcal{F} \frac{\partial \tilde{\gamma}}{\partial z} = \frac{-i}{\hbar D} [\tilde{\gamma} \Delta \tilde{\gamma} + 2E\tilde{\gamma} - \Delta^*], \quad (14)$$

where \mathcal{F} and $\tilde{\mathcal{F}}$ can be read off from Eqs. (4) and (11). As the equations above constitute two coupled second-order differential equations, the full solution requires appropriate boundary conditions. For that purpose, we utilize the general boundary conditions based on the microscopic S-matrix approach suited for diffusive systems that have been developed in Ref. [92]. However, before we discuss them, let us provide a brief overview of the Usadel theory for the case of strong spin splitting, which turns out to be crucial for the geometric effects presented in this work.

B. Strongly spin-polarized materials

Ferromagnetism can be included in the quasiclassical theory by different means. For the limit of weak spin polarization, i.e., $J \lesssim 0.1E_F$, the exchange field can be directly incorporated in the Usadel equation [see Eq. (6)] as a self energy that effectively leads to a spin-dependent energy shift $E \rightarrow E + \mathbf{J} \cdot \boldsymbol{\sigma}$ [93–95]. However, for strongly spin-polarized materials that exceed this limit an alternative approach is needed. Such an approach was proposed in Ref. [12], and is based on the consideration of the strong spin polarization prior to the quasiclassical approximation. In this case one defines two separate Green's function for the two spin bands maintaining the phase coherence within each of them but not between them. Only equal-spin ($\uparrow\uparrow$ and $\downarrow\downarrow$) correlations with respect to a quantization axis parallel to \mathbf{J} are kept whereas the mixed ones are neglected. The validity of such an approximation can be justified by considering the relevant length scales in mesoscopic superconductivity. Namely, as it is known, the mixed-spin correlations with total spin projection $s_z = 0$ exponentially decay on length scales set by the ferromagnetic exchange length $\sim \sqrt{\hbar D / J}$ which for strong spin polarization, $J \sim E_F$, approaches the atomic length scale characterized by the Fermi wavelength λ_F . On the other hand, the relevant length scale for equal-spin triplet correlations with the total spin projection $s_z = \pm 1$ is the thermal coherence length, $\sim \sqrt{\hbar D / k_B T_c}$, which is substantially larger than the exchange length mentioned above.

Taking the above assumptions into account and neglecting the mixed-spin amplitudes in the Green's function [see Eq. (4)], we reduce our problem to two decoupled scalar problems. Namely, each spin band is treated

separately and described by a 2×2 quasiclassical Green's function defined as

$$\check{G}_{\eta\eta} = \begin{pmatrix} \mathcal{G}_{\eta\eta} & \mathcal{F}_{\eta\eta} \\ -\check{\mathcal{F}}_{\eta\eta} & -\check{\mathcal{G}}_{\eta\eta} \end{pmatrix}, \quad (15)$$

where $\eta = \uparrow, \downarrow$ and $\check{\cdot}$ denotes a matrix structure in particle-hole space only. Consequently, the propagators for different spin bands of a ferromagnet obey a diffusive motion described by two decoupled Usadel equations

$$[E\check{\tau}_3, \check{G}_{\eta\eta}] - i\hbar D_\eta \frac{\partial}{\partial z} \left(\check{G}_{\eta\eta} \frac{\partial}{\partial z} \check{G}_{\eta\eta} \right) = \check{0}, \quad \check{G}_{\eta\eta}^2 = \check{1}.$$

Note that the gap matrix vanishes since there is no BCS pairing in the ferromagnet and, in contrast to the previous considerations, the Fermi velocities and the densities of states at the Fermi level are spin-dependent, as is the diffusion constant D_η .

Finally, the transport equation for the coherence functions [see Eqs. (13) and (14)] follows as:

$$\frac{\partial^2 \gamma_{\eta\eta}}{\partial z^2} + \frac{\partial \gamma_{\eta\eta}}{\partial z} \check{\mathcal{F}}_{\eta\eta} \frac{\partial \gamma_{\eta\eta}}{\partial z} = \frac{-i}{\hbar D_\eta} 2E \gamma_{\eta\eta}, \quad (16)$$

and the equation for $\check{\gamma}_{\eta\eta}$ is obtained by applying the $\check{\cdot}$ -operation to the above equation.

Since the ferromagnet (sFM) is characterized by two independent Green's function it is convenient to decompose the currents [see Eqs. (9) and (10)] into their contributions from each spin-band,

$$I_{\text{charge}} = 2e(I_{\uparrow\uparrow} + I_{\downarrow\downarrow}), \quad I_{\text{spin}} = \hbar(I_{\uparrow\uparrow} - I_{\downarrow\downarrow}),$$

and define $I_{\text{ch}} = I_{\uparrow\uparrow} + I_{\downarrow\downarrow}$ and $I_{\text{sp}} = I_{\uparrow\uparrow} - I_{\downarrow\downarrow}$. Here, the exchange field of the sFM sets the global quantization axis (σ_z -axis) and $I_{\eta\eta}$ is given by

$$I_{\eta\eta} = N_{F\eta} D_\eta \text{Re} \int_{-\infty}^{\infty} \frac{dE}{8} \text{Tr} \left\{ \check{\tau}_3 \check{G}_{\eta\eta} \partial_z \check{G}_{\eta\eta} \right\} \tanh \frac{E}{2k_B T}, \quad (17)$$

with Tr denoting the trace over particle-hole space only. Finally, in terms of the coherence functions, the trace in the expression above can be rewritten as [96]

$$2 \left[\{N(\partial_z \gamma) \check{N}, \check{\gamma}\} - \{\check{N}(\partial_z \check{\gamma}) N, \gamma\} \right]_{\eta\eta}, \quad (18)$$

where the subscript $\eta\eta$ indicates that all symbols refer to spin-band η , and $\{\cdot, \cdot\}$ is the anticommutator.

III. SYSTEM UNDER STUDY

We study a superconducting heterostructure consisting of a strongly spin-polarized ferromagnet (sFM) sandwiched between two superconducting leads (SC), separated by ferromagnetic insulating barriers (FI_{1/2}) as sketched in Fig. 1. At the outer interfaces the superconducting leads are linked to two bulk superconductors via highly transparent interfaces, defining the phase bias across the junction. A microscopic description of each magnetically active region is presented in the following.

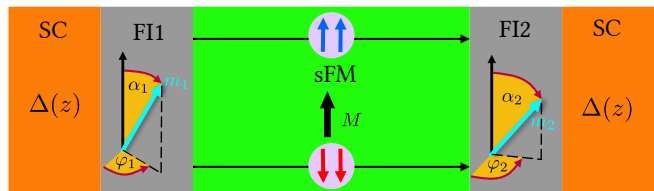


FIG. 1. Sketch of the system under study where two superconductors (SC; orange) are brought into contact with a strongly spin-polarized ferromagnet (sFM; green) via two ferromagnetic insulating barriers (FI1/FI2; grey). At the outer interfaces the system is connected to superconducting reservoirs characterized by the respective pair potential $\Delta_{1/2} = |\Delta_{1/2}| e^{i\chi_{1/2}}$, where 1/2 corresponds to the left/right interface.

A. Strongly spin-polarized ferromagnets

All ferromagnetic parts are modelled by parabolic bands with spin splitting, i.e., the ferromagnetic order in each subsystem is characterized by a respective exchange field \mathbf{J} and a bias potential V . Therefore, the single-particle dispersion relation in the ferromagnet reads

$$\xi_\eta(\mathbf{p}) = \frac{\mathbf{p}^2}{2m} - E_F + V_{\text{sFM}} \mp J_{\text{sFM}}/2, \quad (19)$$

where $\eta = \uparrow, \downarrow$, and the upper sign corresponds to $\eta = \uparrow$. Since we consider strongly spin-polarized ferromagnets, an important aspect at the SF interfaces is the Fermi surface mismatch created by the strong spin splitting. For definiteness, we consider spherical Fermi surfaces but in general this model can be straight-forwardly extended to non-spherical ones. Sketches of the dispersion relations and the Fermi surfaces of an SC/sFM interface are shown in Fig. 2. This model allows to express the Fermi velocity of each spin band in the sFM in terms of the Fermi velocity of the superconductor

$$v_{F,\eta} = v_F \cdot \sqrt{1 - (V_{\text{sFM}} \mp J_{\text{sFM}}/2)/E_F}, \quad (20)$$

which defines $D_\eta = v_{F,\eta}^2 \tau / 3$ in Eq. (16).

B. Spin-polarized interfaces

We now discuss the spin-active interfaces between the superconductors and the central ferromagnetic region. It is important to emphasize that the barrier regions are of thicknesses and energies comparable to the Fermi wave length λ_F and the Fermi energy E_F , respectively, and therefore they enter quasiclassical theory as boundary conditions [13, 94, 97–100], which for diffusive systems and arbitrary spin splittings were derived in Ref. [92]. Thus, the interfaces are characterized by the corresponding normal-state scattering matrix connecting the Bloch waves on the two sides of the interface [101–103]. The S-matrix approach is fully quantum and the microscopic

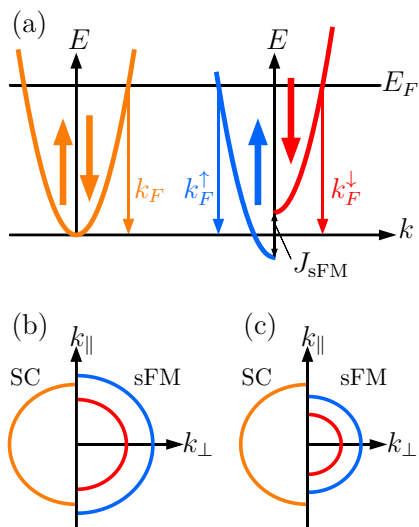


FIG. 2. (a): Schematic representation of the parabolic band model. The SC (left; orange) has a spin-degenerate Fermi surface, whereas the sFM (right) has a separate Fermi surface for each spin band (blue \uparrow , red \downarrow). Two possible Fermi surface geometries are (b) $k_F^\perp < k_F < k_F^\perp$ and (c) $k_F^\perp < k_F^\perp < k_F$.

model of the barrier region is similar to that for the ferromagnetic layer. However, the key distinction is that the interfaces are insulating, i.e., $E_F < V_B \mp J_B/2$. The scattering barriers are modeled as box-shaped potentials schematically shown in Fig. 3. Consequently, the barrier's transparency for each spin-channel is fully determined by its spin-dependent thickness d_η and bias potential V_η^B . In addition, the assumption of spin-dependent barrier widths is a first-order approximation to the case of smooth barrier potentials, see Ref. [104], allowing for a higher spin-mixing angle on the superconducting side of the interface. Due to the spin-splitting, the barriers possess a nonvanishing magnetic moment pointing, in general, in an arbitrary direction with respect to the global quantization axis set by the magnetization vector in the sFM. Accordingly, we parameterize the barrier's magnetic moment direction by the spherical angles α and φ as shown in Fig. 1. Consequently, the barriers are fully described by the set of following parameters: V , J , $d_{\uparrow,\downarrow}$, α , and φ . Finally, the S-matrix of an SC/sFM interface discussed above has a general 4×4 matrix structure

$$S = \begin{pmatrix} R_{SC} & T_{\uparrow}^{SC \leftarrow sFM} & T_{\downarrow}^{SC \leftarrow sFM} \\ T_{\uparrow}^{sFM \leftarrow SC} & r_{\uparrow} & r_{\uparrow\downarrow} \\ T_{\downarrow}^{sFM \leftarrow SC} & r_{\downarrow\uparrow} & r_{\downarrow} \end{pmatrix}, \quad (21)$$

where R_{SC} is a 2×2 block describing reflection processes (normal and spin-flip) on the superconducting side. Transmission events are described by the row- ($T_{\uparrow}^{sFM \leftarrow SC}, T_{\downarrow}^{sFM \leftarrow SC}$) or column-vectors ($T_{\uparrow}^{SC \leftarrow sFM}, T_{\downarrow}^{SC \leftarrow sFM}$), which characterize transmission of

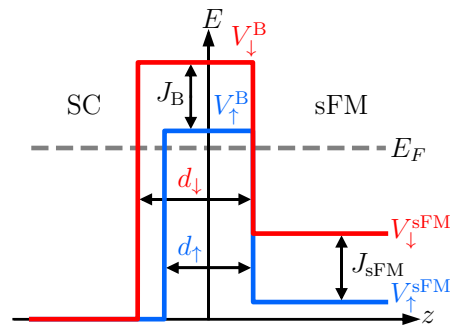


FIG. 3. A schematic representation of the potentials characterizing the SC/sFM interface in our model. In the superconductor (SC) it is assumed that no bias potentials and exchange fields are present. In the ferromagnetic insulator both spin bands are shifted above the Fermi energy and are therefore insulating whereas in the strongly spin-polarized ferromagnet the bands are splitted but metallic. Since the splitting in both magnetic materials is of the order of E_F the Fermi surfaces are split, see Fig. 2. The potentials in the two regions for each spin direction are given by $V_{\uparrow(\downarrow)}^{B/sFM} = V^{B/sFM} \mp J^{B/sFM}/2$, where it is ensured that $V_{\uparrow(\downarrow)}^B > E_F$ and $V_{\uparrow(\downarrow)}^{sFM} < E_F$.

Bloch waves from region A to B ($B \leftarrow A$). Finally, the reflection processes on the sFM side are characterized by r_η and $r_{\eta\bar{\eta}}$.

IV. BOUNDARY CONDITIONS

For solving a specific problem the Usadel equation (6) needs to be supplemented with boundary conditions appropriate for the system at hand. As previously mentioned, the case of ferromagnetic insulating barrier layers can be implemented by considering the general boundary conditions derived in Ref. [92] for which we utilise the scattering matrix calculated in the last section. In what follows, we outline the three-set procedure described in detail in Ref. [92] but use a modified notation which yields a simplification of the equations therein.

Since we assume the conservation of momentum parallel to the interface [see Fig. 2] we can label the scattering channels by their respective parallel momentum p_\parallel . Consequently, all quantities in the following are functions of p_\parallel , but we omit the explicit dependence when it is not explicitly needed. Following Ref. [92], we first decompose S into a polar decomposition

$$S = \begin{pmatrix} \sqrt{1 - CC^\dagger} & C \\ C^\dagger & -\sqrt{1 - C^\dagger C} \end{pmatrix} \begin{pmatrix} S & 0 \\ 0 & \underline{S} \end{pmatrix}, \quad (22)$$

where the entries on the right hand side are matrices in spin space. The block diagonal matrix $\text{diag}(S, \underline{S})$, represents an auxiliary scattering matrix for an impenetrable interface and C is a generalised transmission matrix. In the following, we derive a more compact version of the boundary conditions in Ref. [92] by utilizing the principal

matrix square root of S , which we denote by $\mathcal{S} = \sqrt{S}$, and similarly $\underline{\mathcal{S}} = \sqrt{S}$.

We parameterize C by a hopping matrix τ through the barrier as follows:

$$C = \mathcal{S}(1 + \tau\tau^\dagger)^{-1}2\tau\underline{\mathcal{S}}^\dagger. \quad (23)$$

Hopping in the opposite direction is given by $\underline{\tau} = \tau^\dagger$. The particle-hole structure of the scattering and hopping matrices are, respectively,

$$\hat{S}(p_\parallel) = \begin{pmatrix} \mathcal{S}(p_\parallel) & 0 \\ 0 & \mathcal{S}^T(-p_\parallel) \end{pmatrix}, \quad (24)$$

$$\hat{\tau}(p_\parallel) = \begin{pmatrix} \tau(p_\parallel) & 0 \\ 0 & \underline{\tau}^T(-p_\parallel) \end{pmatrix}. \quad (25)$$

The derivation in Ref. [92] assumes separation of the space around the scattering barrier into a diffusive zone, an isotropization zone, and a ballistic region directly around the scattering barrier. The procedure proceeds by implementing an idea based on Refs. [98] and [105], where it was shown that a scattering problem at a perturbation field can be solved by using an auxiliary Green's function \hat{g}_0 . This Green's function is the solution of the problem in the absence of the perturbation field but the self-energies are the same as before. In our case such a situation is realized by considering an impenetrable interface allowing us to calculate the transmission matrix \hat{t} . To do so, we first need to account for \hat{g}_0 which in the considered case can be directly calculated from the diffusive propagator \hat{G} . We first introduce two new diffusive propagators

$$\hat{G}_1 = \hat{S}\hat{G}\hat{S}^\dagger \quad \text{and} \quad \hat{G}_2 = \hat{S}^\dagger\hat{G}\hat{S}.$$

expressing \hat{g}_0 as follows [92]:

$$\hat{g}_0 = 2(\hat{1} + \hat{G}_1\hat{G}_2)^{-1}(\hat{1} + \hat{G}_1) - \hat{1}. \quad (26)$$

Note that even though \hat{G} does not depend on the momentum of the incident particle, $\hat{G}_{1,2}$ as well as the ballistic auxiliary propagator \hat{g}_0 are functions of p_\parallel , which is encoded in \hat{S} .

The next step is to calculate the t -matrix which allows to connect the ballistic propagators on either side of the interface. The t -matrix follows from the solution of a Dyson-like equation for \hat{g}_0 and reads

$$\hat{t} = (\hat{1} + \hat{g}_1\hat{g}_0)^{-1}\hat{g}_1, \quad (27)$$

where $\hat{g}_1 = \hat{\tau}\hat{g}_0\hat{\tau}^\dagger = \hat{\underline{\tau}}^\dagger\hat{g}_0\hat{\underline{\tau}}$. Finally, \hat{t} is used for calculating the incoming, \hat{g}_i , and outgoing propagators, \hat{g}_o , on one side of the scattering barrier

$$\hat{g}_i = \hat{S}^\dagger [\hat{g}_0 - (\hat{g}_0 - \hat{1})\hat{t}(\hat{g}_0 + \hat{1})] \hat{S}, \quad (28)$$

$$\hat{g}_o = \hat{S} [\hat{g}_0 - (\hat{g}_0 + \hat{1})\hat{t}(\hat{g}_0 - \hat{1})] \hat{S}^\dagger. \quad (29)$$

The difference between these is referred to as the matrix current $\hat{\mathcal{I}}$, which characterizes the transmission and reflection of correlations through/at the barrier, $\hat{\mathcal{I}} = \hat{g}_o - \hat{g}_i$.

As introduced in Ref. [106], the boundary conditions for the diffusive propagators are

$$\mathcal{G}_q \sum_{n=0}^{\mathcal{N}_{\max}} \hat{\mathcal{I}}_{nn} = -\frac{\sigma\mathcal{A}}{\xi} \hat{G} \frac{\partial}{\partial z} \hat{G}, \quad (30)$$

where n is the channel index, $\mathcal{G}_q = e^2/h$ the quantum of conductance, $\sigma = e^2 N_F D$ is the normal state conductivity per spin, \mathcal{A} the surface area of the contact, ξ the corresponding coherence length of the system, and z the coordinate parallel to the interface normal. In the limit of strong polarization σ and ξ become spin-dependent quantities which can be accounted for by redefining them as matrices acting only in spin space. The transition from discrete channel index to the conserved parallel momentum k_\parallel can be done by [92]

$$\frac{1}{\mathcal{N}_{\max}} \sum_{n=0}^{\mathcal{N}_{\max}} \dots = \frac{1}{A_{F,z}} \int_{A_{F,z}} d^2 k_\parallel \dots \quad (31)$$

This relation allows to rewrite the boundary conditions as

$$\hat{\underline{\mathcal{I}}} \equiv \langle \hat{\mathcal{I}}(k_\parallel) \rangle_{A_{F,z}} = -\frac{\mathcal{G}_N}{\mathcal{G}_B} \hat{G} \frac{\partial}{\partial z} \hat{G} = -r \hat{G} \frac{\partial}{\partial z} \hat{G}, \quad (32)$$

where $\langle \dots \rangle_{A_{F,z}} = A_{F,z}^{-1} \int_{A_{F,z}} d^2 k_\parallel \dots$, $A_{F,z}$ is the projection of the Fermi surface onto the plane perpendicular to the barrier, $\mathcal{G}_N = \sigma\mathcal{A}/\xi$ the normal state conductance of the subsystem, and $\mathcal{G}_B = \mathcal{G}_q \mathcal{N}_{\max}$ the conductance of the barrier. The ratio between \mathcal{G}_N and \mathcal{G}_B is denoted as $r = \mathcal{G}_N/\mathcal{G}_B$ in the following. All of the above equations also hold for the propagators on the opposite side of the barrier. The transition is made by interchanging the underlined and the not underlined quantities.

Since we use coherence functions which parameterise the Green's function, the above boundary conditions should be adapted to this parameterization. One way for doing so was presented in Ref. [107], but here we choose a different approach based on the projector formalism [83, 108]. The projectors are defined as

$$2\hat{P}_\pm = \hat{1} \pm \hat{G}, \quad (33)$$

allowing to rewrite Eq. (32) as

$$-2r\hat{P}_\pm \frac{\partial \hat{P}_\pm}{\partial z} \hat{P}_\mp = \hat{P}_\pm \hat{\underline{\mathcal{I}}}. \quad (34)$$

This equation allows to obtain 2 boundary conditions for each γ and $\tilde{\gamma}$. The equivalence of each of the two equations as well as the equivalence to the boundary conditions calculated in Ref. [107] can be shown by considering the symmetry relations implied by Eq. (34), i.e., $\hat{P}_\pm \hat{\underline{\mathcal{I}}} \hat{P}_\pm = \hat{0}$. One set of boundary conditions following from Eq. (34) is

$$\begin{aligned} -2r \frac{\partial \gamma}{\partial z} &= (\bar{\mathcal{I}}_{12} + \gamma \bar{\mathcal{I}}_{22})(1 - \tilde{\gamma} \gamma), \\ -2r \frac{\partial \tilde{\gamma}}{\partial z} &= (\bar{\mathcal{I}}_{21} + \tilde{\gamma} \bar{\mathcal{I}}_{11})(1 - \gamma \tilde{\gamma}), \end{aligned} \quad (35)$$

where the particle-hole structure of the matrix current is

$$\hat{\mathcal{I}} = \begin{pmatrix} \bar{\mathcal{I}}_{11} & \bar{\mathcal{I}}_{12} \\ \bar{\mathcal{I}}_{21} & \bar{\mathcal{I}}_{22} \end{pmatrix}. \quad (36)$$

Finally, we remark that the boundary conditions in Eq. (35) can be used for a variety of matrix currents, i.e. the matrix current from Nazarov's boundary conditions [106] or the matrix current for the boundary conditions of Kuprianov and Lukichev [109].

V. RESULTS

In this section we present the results of our numerical calculations of an SC/FI/sFM/FI/SC hybrid junction described in the previous sections. Having obtained the quasiclassical Green's functions as the solutions of the Usadel equation [see Eq. (16)] supplemented by the boundary conditions introduced in Sec. IV, we account for the Josephson current-phase relation in the strongly spin-polarized ferromagnet for both the charge, I_{charge} , and the spin current, I_{spin} .

In what follows we discuss the Josephson current as a function of the superconducting phase difference, $\Delta\chi = \chi_2 - \chi_1$, and the geometric phase difference, $\Delta\varphi = \varphi_2 - \varphi_1$ (the subscripts 1/2 correspond to the left/right interface), defined by the relative orientation between the magnetizations of the three ferromagnetic regions discussed below in more detail. Our main objective here is to provide a systematic theoretical study of the Josephson diode effect.

As mentioned previously, the quantity typically used to quantify this effect is the diode efficiency, defined as

$$\eta_x(\Delta\varphi) = \frac{|I_x^+| - |I_x^-|}{|I_x^+| + |I_x^-|}, \quad (37)$$

where $x = \text{ch, sp}$ refers to the charge and the spin diode efficiency, respectively, and $I_x^\pm \equiv I_x(\Delta\chi_{\text{ch}}^\pm)$. Here, $\Delta\chi_{\text{ch}}^\pm$ are the superconducting phase differences at which the positive (+) or negative (-) critical charge current is reached for fixed $\Delta\varphi$, i.e., $\Delta\chi_{\text{ch}}^+ = \text{argmax}_{\Delta\chi}(I_{\text{ch}})$ and $\Delta\chi_{\text{ch}}^- = \text{argmin}_{\Delta\chi}(I_{\text{ch}})$. We use a definition for the spin diode efficiency that refers to the Josephson phases at the critical charge currents, as it is the charge current that usually can be controlled externally [110]. As we will show below, a geometric contribution independent of $\Delta\chi$ dominates the Fourier decomposition of the spin current in strongly asymmetric Josephson junctions of the type we consider here. In this case, a spin Josephson diode efficiency based on the extremal positive and negative spin currents, as in Ref. [111], would yield almost everywhere 100%, even if one of the two interfaces were entirely intransparent. The definition of Eq. (37) we use here is directly related to the Josephson effect in both charge and spin channel, and allows us to study the diode efficiency as a function of the system's parameters, among which the geometric phase $\Delta\varphi$ plays a crucial role. In

particular, as we qualitatively discuss in Sec. I and confirm quantitatively below, the key feature leading to the Josephson diode effect is the noncoplanarity of the three magnetizations in the system $(\mathbf{m}_1, \mathbf{m}_2, \mathbf{M})$. Mathematically this condition is expressed as $(\mathbf{m}_1 \times \mathbf{m}_2) \cdot \mathbf{M} \neq 0$. By assuming $\mathbf{M} = |\mathbf{M}|e_z$ and parametrizing the misalignment of the other two magnetizations with respect to \mathbf{M} by spherical angles [see Fig. 1], the latter relation translates into $|\mathbf{m}_1||\mathbf{m}_2||\mathbf{M}| \sin(\alpha_1) \sin(\alpha_2) \sin(\Delta\varphi) \neq 0$. In other words, the noncoplanarity condition crucially depends on the relative azimuthal angle $\Delta\varphi = \varphi_2 - \varphi_1$ which we term the geometric phase difference and on the polar misalignment characterized by the α_i 's.

A. Numerical procedure

The results in this work are obtained by employing the following numerical procedure. For each point in the two-dimensional $(\Delta\chi, \Delta\varphi)$ -plane we iterate the nonlinear spin-dependent Usadel equations for the quasiclassical Green's function, the self-consistency relation for the spatially dependent superconducting order parameter, as well as the nonlinear spin-dependent boundary conditions until convergence is achieved. We then obtain the self-consistent current-phase relations, determine the global maxima and minima, and calculate the charge and spin Josephson diode efficiencies. These last steps are greatly facilitated by a two-dimensional numerical Fourier decomposition of the current phase relations as function of $\Delta\chi$ and $\Delta\varphi$. We also analyse the current-phase relations in order to obtain spontaneous currents in a loop geometry and a switching effect between nearly 100% spin-polarized supercurrents. Finally, we calculate the local density of states in the superconductor and in the ferromagnet.

B. Current-phase relations and diode efficiencies

In the following, we discuss the Josephson current-phase relations and the diode efficiencies, η_x , for the cases of symmetric and asymmetric junctions. Before presenting the numerical results, we briefly discuss the scaling. As it is known from mesoscopic physics, the typical energy and lengths scales in quasiclassical superconductivity are the superconducting transition temperature, $k_B T_c$, and the coherence length $\xi = \sqrt{\hbar D / (k_B T_c)}$, respectively. On the contrary, the energy scale related to the exchange splitting, in both the sFM and the ferromagnetic interfaces, and the length scale related to the ferromagnetic interfaces are expressed in the units of the Fermi energy E_F and wavelength λ_F , which are beyond the quasiclassical theory. All results for the spin-resolved currents and thus for I_{ch} and I_{sp} are expressed in the units of $I_0 = k_B T_c / (e^2 R_N)$. Here, $R_N^{-1} = \sigma_N \sqrt{\mathcal{T}_L^\uparrow \mathcal{T}_L^\downarrow} \sqrt{\mathcal{T}_R^\uparrow \mathcal{T}_R^\downarrow}$ with $\mathcal{T}_{L/R}^{\uparrow(\downarrow)}$ being the trans-

mission probability of the left/right barrier for the spin- \uparrow or spin- \downarrow channel in the case of perpendicular impact, and $\sigma_N = e^2 N_F D$ is the normal state conductivity of the superconductors.

Most of the results in this work are obtained for the temperature $T = 0.1T_c$, superconducting layer's thicknesses $L_S = 5\xi$, barrier conductivity ratios $r = 1$, ferromagnetic layer's thickness $L = \xi$. Magnetization direction of the ferromagnet $\mathbf{M} \parallel \mathbf{e}_z$ and polar angle characterizing the left and right interfaces' magnetizations $\alpha_L = \alpha_R = \pi/2$ [see Fig. 1], i.e., \mathbf{m}_1 and \mathbf{m}_2 lie in the $x - y$ plane. To get more insights into the role of these parameters we refer to Appendix C.

We first discuss the Josephson effect occurring in the case of coplanar magnetizations and symmetric interfaces. Such a configuration is realized for the cases $\sin(\Delta\varphi) = 0 \implies \Delta\varphi = k\pi, k \in \mathbb{Z}$. The resulting current-phase relations calculated for $\Delta\varphi = 0$ are shown in Fig. 4(a), where the dashed lines represent the spin-resolved currents whereas the solid green line represents the charge current. The system's parameters are shown in the caption. The corresponding spin current is represented by the dashed line in Fig. 4(c) and it is well-approximated by the standard sinusoidal shape. Note that in this case, all currents exhibit the normal Josephson effect, $I(\Delta\chi) = -I(-\Delta\chi)$.

However, the situation of nonvanishing $\Delta\varphi$, i.e., a non-coplanar configuration, drastically modifies the Josephson current-phase relation as shown in Fig. 4(b). The curves are calculated for $\Delta\varphi = 0.44\pi$ and other parameters being the same as in Fig. 4(a). There are two new phenomena compared to the coplanar case. First, the anomalous Josephson effect, characterized by $I(\Delta\chi = 0) \neq 0 \implies I(\Delta\chi) \neq -I(-\Delta\chi)$, occurs. Second, the presence of higher harmonics gives rise to the Josephson diode effect for the charge current (green solid line). This effect is explicitly visible in Fig. 4(d) where the absolute value of the charge current from (b) is plotted. The spin current [solid line in Fig. 4(c)] displays a current-phase relation strongly shifted in $\Delta\chi$ compared to the coplanar case [dashed line in Fig. 4(c)]. A detailed analysis of the diode efficiencies and the harmonic decomposition of the current-phase relation for charge and spin currents is provided below.

To obtain a better insight in the role of the geometric phase difference, we consider the charge and the spin current (quantified by $I_{\text{ch}} = I_{\uparrow\uparrow} + I_{\downarrow\downarrow}$, $I_{\text{sp}} = I_{\uparrow\uparrow} - I_{\downarrow\downarrow}$) as a function of $\Delta\chi$ and $\Delta\varphi$, shown in Figs. 5(a) and 5(b), respectively. Both panels are plotted for the same selection of parameters as in Fig. 4. Apparently, $I_{\text{ch}}(\Delta\chi)$ has significant contributions from higher harmonics except for $\Delta\varphi \approx k\pi$, $k \in \mathbb{Z}$ where the first harmonic is dominant, i.e., $I_{\text{ch}} \approx I_{\text{ch}}^{\pm}(\Delta\varphi) \sin(\Delta\chi)$. In addition, we observe $\Delta\varphi$ -driven $0 - \pi$ transitions. The spin current, shown in panel (b), is for most values of $\Delta\varphi$ well-approximated by $I_{\text{sp}} \sim \pm \cos(\Delta\chi)$. Panels (c) and (d) show the charge η_{ch} (green) and the spin η_{sp} (violet) diode efficiency, respectively, as a function of $\Delta\varphi$, obtained from a numerical

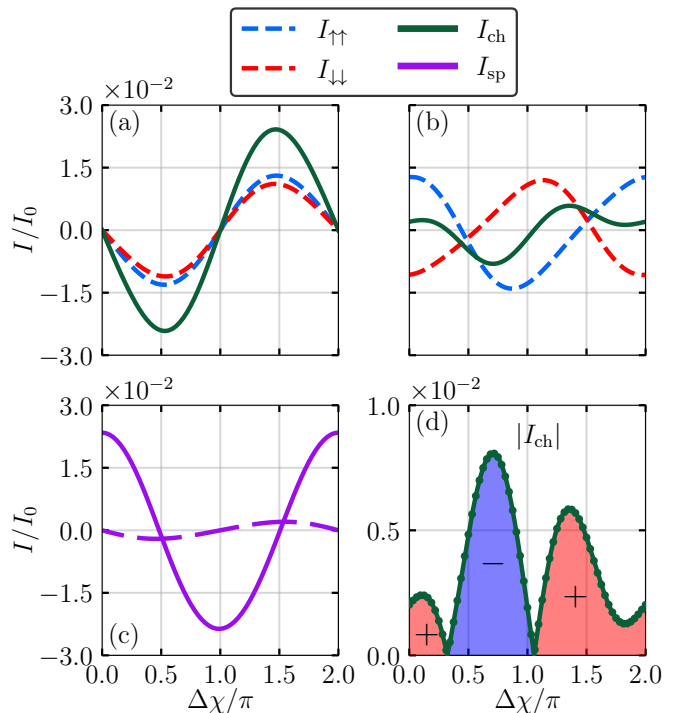


FIG. 4. Spin-resolved current-phase relation (CPR) $I_{\uparrow\uparrow}(\Delta\chi)$, $I_{\downarrow\downarrow}(\Delta\chi)$, and charge current $I_{\text{ch}}(\Delta\chi)$ for (a) a coplanar arrangement of $(\mathbf{m}_1, \mathbf{m}_2, \mathbf{M})$, i.e., $\Delta\varphi = 0$, and (b) a non-coplanar arrangement, here $\Delta\varphi/\pi = 0.44$. (c) spin currents $I_{\text{sp}}(\Delta\chi)$ corresponding to panel (a) and (b) for the coplanar case (dashed line) and the noncoplanar case (solid line). (d) absolute value of I_{ch} from panel (b), with the sign denoted by red (+) and blue (-) color; dots represent values calculated via QCGFs and used for the Fourier decomposition of the CPR. Parameters are appropriate for a symmetric junction with $V_B = 1.3E_F$, $V_{\text{sFM}} = 0$, $J_{\text{sFM}} = J_B = 0.4E_F$, $d_{\uparrow} = 0.6\lambda_F/2\pi$ and $d_{\downarrow} = 0.8\lambda_F/2\pi$. The left and the right barrier differ only in φ .

Fourier decomposition of the currents shown in panels (a) and (b). We find a significant diode effect in both the charge and the spin current, and obtain a perfect spin diode for distinct $\Delta\varphi$'s, i.e., $\eta_{\text{sp}} = \pm 1$. The diode effect vanishes for $\Delta\varphi = k\pi$, which corresponds to the case of a coplanar spin arrangement. The diode effect vanishes also for $\Delta\varphi = \frac{\pi}{2} + k\pi$. This can be explained by considering the phase-factors acquired by $\uparrow\uparrow$ and $\downarrow\downarrow$ correlations which either coincide for $\Delta\varphi = k\pi$ or differ by multiples of π for $\Delta\varphi = \frac{\pi}{2} + k\pi$. Also, η_{ch} tends to peak around $\Delta\varphi = \frac{\pi}{2} + k\pi$, whereas perfect efficiency in η_{sp} can occur for any $\Delta\varphi$ differing from $k\frac{\pi}{2}$, as shown in Appendix C. In Fig. 5 it happens to be close to $\Delta\varphi = k\pi$.

Changing the parameters characterising the strong spin-splitting yields a change in the magnitude and the explicit functional dependencies, however the effect itself is present as long as the barriers and the sFM are spin-active, and the sFM has two itinerant spin bands (i.e., is not half-metallic) with different densities of states. For a discussion of the effect over a wide range of parameters

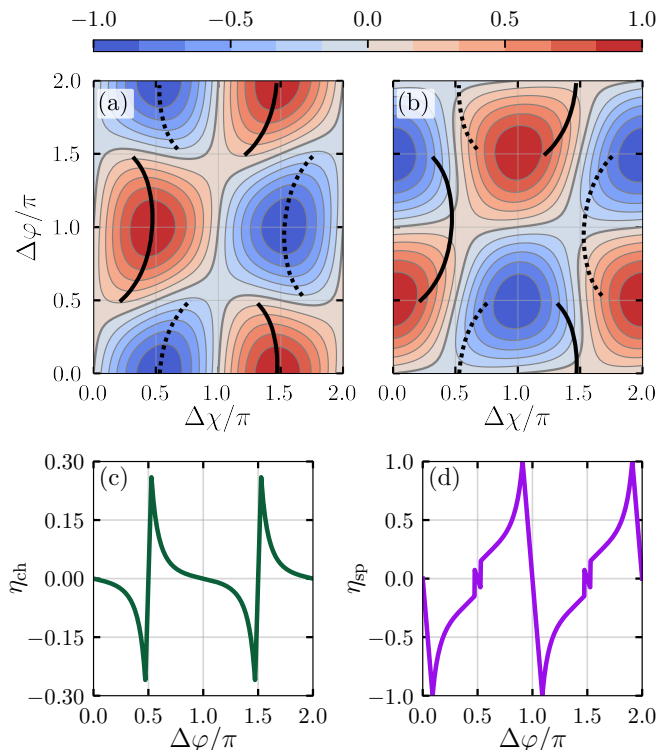


FIG. 5. Functional dependence of (a) charge, I_{ch} , and (b) spin current, I_{sp} , of a symmetric junction on the superconducting phase difference $\Delta\chi$ and the geometric phase $\Delta\varphi$. Currents in each panel are normalized to their maximal values. Solid black and dashed lines show the branches of $\Delta\chi^+(\Delta\varphi)$ and $\Delta\chi^-(\Delta\varphi)$ [see the text for definition], respectively. The thick grey line in (a) and (b) denotes zero current. In (c) and (d) the functional dependence of the charge and spin diode efficiency on $\Delta\varphi$ is shown. The potentials and exchange fields of the barrier and bulk ferromagnet are the same as in Fig. 4.

see Appendix C.

In the previous discussion, we assumed that both interfaces in the system are identical up to different φ 's. We now briefly discuss the case of different barrier widths, i.e., different transmission probabilities on either side of the sFM. For definiteness, we use the same parameters as in Fig. 4 except that now the right barrier is less transparent having the width $d_R = 4.16\lambda_F/2\pi$ (for both spin projections). Figure 6(a) shows the spin current I_{sp} as a function of the superconducting, $\Delta\chi$, and the geometric phase difference, $\Delta\varphi$, whereas Fig. 6(b) shows the corresponding spin diode efficiency as function of $\Delta\varphi$. In this case, higher harmonics of the charge current are strongly suppressed and the Josephson current-phase relation is approximately sinusoidal. On the other hand, the spin current $I_{\text{sp}}(\Delta\chi, \Delta\varphi)$ does not change its sign as a function of $\Delta\chi$ in a wide range of $\Delta\varphi$. We observe sign changes with $\Delta\chi$ only in relatively narrow ranges of $\Delta\varphi$ close to $\Delta\varphi \approx \frac{\pi}{2} + k\pi$. The spin Josephson efficiency, shown in Fig. 6(b), exhibits the perfect efficiency only close to $\Delta\varphi \approx \frac{\pi}{2} + k\pi$, and extremely close to $\Delta\varphi \approx k\pi$. A more detailed discussion on the cross-over from sym-

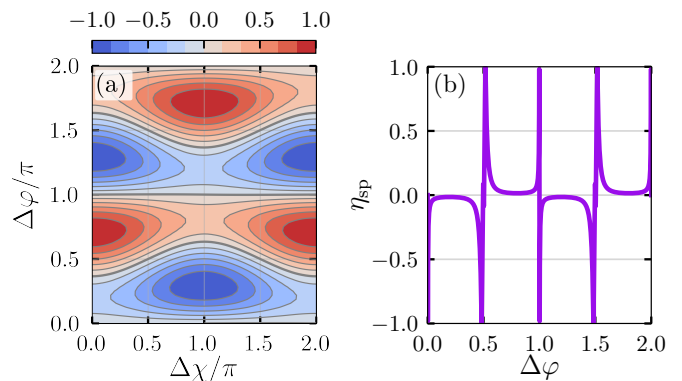


FIG. 6. (a) Spin current, I_{sp} , and (b) spin diode efficiency, η_{sp} , as in Fig. 5(b) and (d), however for an asymmetric junction where the left barrier is the same as in the symmetric case (see Fig. 4) and for the right barrier the barrier width is the same for both spin projections, $d_R = 4.16\lambda_F/2\pi$. The remaining parameters are the same as in Fig. 4.

metric to strongly asymmetric junctions can be found in Appendix C.

C. Fourier decomposition

As already indicated, the presence of higher harmonics in the Josephson current-phase relation is crucial for the Josephson diode effect. To get more insight, we present a detailed Fourier analysis of the current-phase relation both in $\Delta\chi$ and $\Delta\varphi$. Since both the charge, I_{ch} , and the spin current, I_{sp} , are mediated by equal-spin triplet contributions, $I_{\eta\eta}$, $\eta = \uparrow, \downarrow$, in this subsection we focus on them separately. We will show below that the current phase relations can be written in the form

$$I_{\uparrow\uparrow} = \frac{1}{2} \sum_{\mu, \nu = -\infty}^{\infty} (-1)^{\mu+\nu} \mu I_{\mu, \nu} \sin \psi_{\mu, \nu}, \quad (38)$$

$$I_{\downarrow\downarrow} = \frac{1}{2} \sum_{\mu, \nu = -\infty}^{\infty} (-1)^{\mu+\nu} \nu I_{\mu, \nu} \sin \psi_{\mu, \nu}, \quad (39)$$

where $I_{-\mu, -\nu} = I_{\mu, \nu}$, and

$$\psi_{\mu, \nu} = (\mu + \nu)\Delta\chi - (\mu - \nu)\Delta\varphi \quad (40)$$

is an *effective Josephson phase*. This form has been suggested for ballistic systems [4, 112], and we show here that it also holds for diffusive systems. Eqs. (38)-(40) have an appealing physical interpretation in terms of transferred equal-spin Cooper pairs across the junction [4]. They present the current-phase relation for the case of a coherent transfer of $\mu \uparrow\uparrow$ and $\nu \downarrow\downarrow$ equal-spin pairs (positive values denote transmissions in positive current direction, negative values denote transmissions in the opposite direction). Taking into account that the ground state for $\Delta\varphi = 0$ is a π -junction, the Josephson phase acquired for a coherent transfer of a single $\uparrow\uparrow / \downarrow\downarrow$ pair

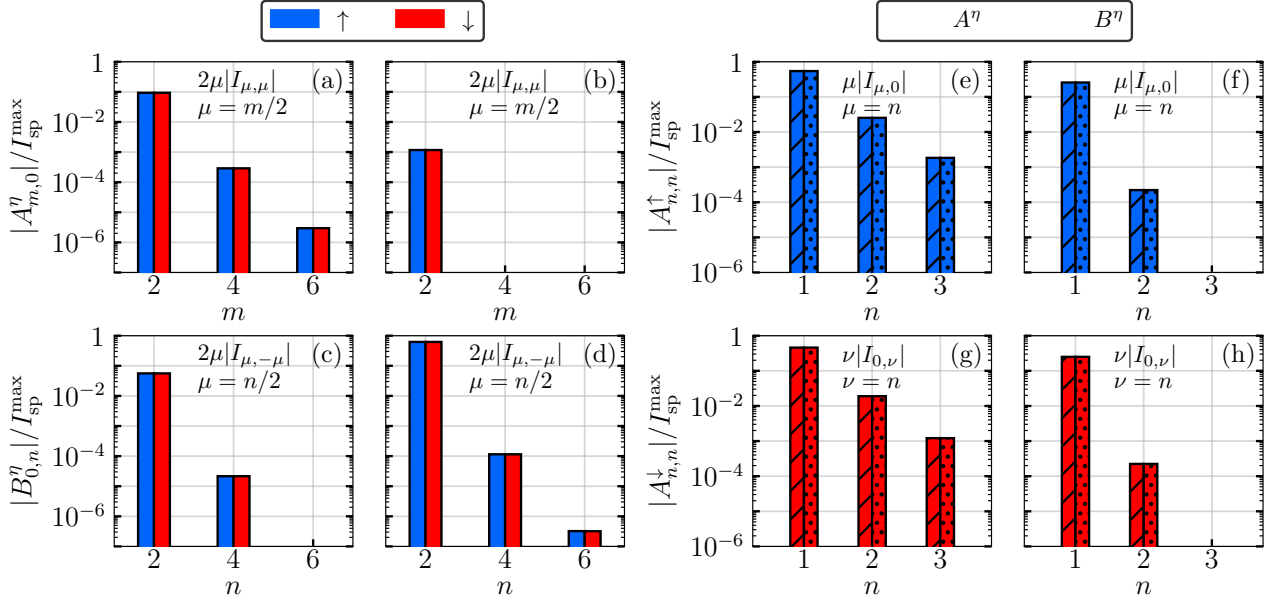


FIG. 7. Fourier components of the spin-resolved currents corresponding to the charge and spin currents shown in panels (a) and (b) of Figs. 5 and 6. The panels (a),(c),(e), and (g) of this figure show the results for the symmetric case [see Fig. 5], whereas the panels (b),(d),(f), and (h) shows the results for the asymmetric junction case [see Fig. 6]. The different colors indicate the two spin-bands for which we perform the Fourier analysis, \uparrow in blue and \downarrow in red. In (a) and (b) we plot the absolute value of the $A_{m,0}^\eta$ component and in panels (c) and (d) the absolute values of the $B_{0,n}^\eta$ components are shown. Panels (e) - (h) show the absolute values of the Fourier components with equal contributions in $\Delta\chi$ and $\Delta\varphi$, i.e. $A_{n,n}^\eta$ (dashed bar) and $B_{n,n}^\eta$ (dotted bar), for the \uparrow -band in panels (e) and (f) and for the \downarrow -band in panels (g) and (h). All Fourier components are normalized to the maximum spin current for the corresponding case, i.e. $I_{sp}^{\max} = \max_{(\Delta\chi, \Delta\varphi)} I_{sp}(\Delta\chi, \Delta\varphi)$.

is $\Delta\chi \pm \Delta\varphi + \pi$. Thus, for the coherent transport of μ $\uparrow\uparrow$ -pairs and ν $\downarrow\downarrow$ -pairs a Josephson phase $\mu(\Delta\chi - \Delta\varphi + \pi) + \nu(\Delta\chi + \Delta\varphi + \pi) = (\mu + \nu)\Delta\chi - (\mu - \nu)\Delta\varphi + (\mu + \nu)\pi$ appears, leading Eqs. (39)-(40). Note that within the system at hand only even numbers of electrons are transmitted through each spin band of the sFM, as short-range pair amplitudes, involving both bands, are negligible for strong spin polarization.

We now proceed to discuss a number of symmetry relations for a general Fourier series expansion that allow us to derive Eqs. (39)-(40) for our system on general grounds. Using the general QCGF technique we numerically confirm these symmetry relations. Details are given in Appendix A. We make use of the fact that $I_{\eta\eta}$ under the time reversal symmetry transforms as follows [4]:

$$I_{\eta\eta}(\Delta\chi, \Delta\varphi) = -I_{\eta\eta}(-\Delta\chi, -\Delta\varphi). \quad (41)$$

This relation is derived by noting that the angle $\Delta\varphi$ is defined by three magnetic vectors that behave odd under time reversal. We also chose as spin quantization axis the magnetization \mathbf{M} in the sFM, and therefore both behave odd under time reversal, allowing for the derivation of the above relation for majority and minority spin bands. A general Fourier series expansion compatible with Eq. (41)

is given by (again, $\eta \in \{\uparrow, \downarrow\}$)

$$I_{\eta\eta} = \frac{1}{2} \sum_{m=1}^{\infty} A_{m,0}^\eta \sin(m\Delta\chi) + \frac{1}{2} \sum_{n=1}^{\infty} B_{0,n}^\eta \sin(n\Delta\varphi) + \sum_{m,n=1}^{\infty} \left[A_{m,n}^\eta \sin(m\Delta\chi) \cos(n\Delta\varphi) + B_{m,n}^\eta \cos(m\Delta\chi) \sin(n\Delta\varphi) \right]. \quad (42)$$

In Appendix A we list symmetry relations between the coefficients $A_{m,n}^\eta$, $B_{m,n}^\eta$ which are confirmed by our numerical calculations, and which render Eq. (42) equivalent to Eqs. (38)-(40). In particular, we find that coefficients are only nonzero when either both m and n are even or both m and n are odd (i.e., when $m \pm n$ is even). Given this fact, the coefficients relating Eq. (39) to Eq. (42) are

$$(-1)^{\mu+\nu} |\mu| I_{\mu,\nu} = \frac{A_{|\mu+\nu|,|\mu-\nu|}^\uparrow - B_{|\mu+\nu|,|\mu-\nu|}^\uparrow}{2}, \quad (43)$$

$$(-1)^{\mu+\nu} |\nu| I_{\mu,\nu} = \frac{A_{|\mu+\nu|,|\mu-\nu|}^\downarrow - B_{|\mu+\nu|,|\mu-\nu|}^\downarrow}{2}, \quad (44)$$

and we define formally $A_{0,2\nu}^\eta = 0$ and $B_{2\mu,0}^\eta = 0$. In the following, we focus on the discussion of the most relevant Fourier contributions $A_{m,0}^\eta$, $B_{0,n}^\eta$, $A_{n,n}^\eta$, and $B_{n,n}^\eta$ which

are presented in Fig. 7, and which correspond to $I_{\mu,\mu}$, $I_{\mu,-\mu}$, $I_{\mu,0}$, and $I_{0,\nu}$, correspondingly.

We start by considering the absolute values of $A_{m,0}^\eta$ [see Figs. 7(a) and 7(b)] and $B_{0,n}^\eta$ [see Figs. 7(c) and 7(d)]. Note that the left column in both cases corresponds to the symmetric junction from Fig. 5 whereas the right one refers to the asymmetric junction considered in Fig. 6. It is evident that in both cases the Fourier components for the \uparrow (red bars) and the \downarrow channel (blue bars) coincide. Furthermore, we obtain a sign change for $B_{0,n}^\eta$ (which is not explicitly visible here since we show the absolute values for better comparison). Thus, the symmetries of these contributions can be summarized as

$$A_{m,0}^\uparrow = A_{m,0}^\downarrow \quad \text{and} \quad B_{0,n}^\uparrow = -B_{0,n}^\downarrow. \quad (45)$$

Only Fourier coefficients of even order are nonzero. The physical interpretation of $\frac{1}{2}A_{2\mu,0}^\eta = \mu I_{\mu,\mu}$ is in terms of crossed pair transmission processes, where in both spin bands μ equal-spin pairs are transferred across the junction in the same direction. These terms are therefore equal for $\eta = \uparrow, \downarrow$ and contribute only to the charge current. On the other hand, $\frac{1}{2}B_{0,2\nu}^\uparrow = \nu I_{\nu,-\nu}$ represent processes where ν equal-spin pairs are transferred in opposite direction for the two spin bands. These terms have opposite signs for opposite spin and therefore contribute only to the spin current. Considering the amplitudes of the Fourier components, which are normalized to the respective maximum spin current, shows that in the symmetric case [see Figs. 7(a) and 7(c)] crossed pair transmission processes of an equal number of Cooper pairs in the two spin bands in the same direction dominate, whereas for the asymmetric case [see Figs. 7(b) and 7(d)] the transmission processes of an equal number of Cooper pairs in the two spin bands in opposite directions dominate.

Next, we discuss the Fourier components with equal contributions from $\Delta\chi$ and $\Delta\varphi$, i.e., $A_{n,n}^\eta$ and $B_{n,n}^\eta$. The absolute values of them are plotted in Figs. 7(e) and 7(f) (\uparrow spin band; blue) and Figs. 7(g) and 7(h) (\downarrow spin band; red). Different patterns corresponds to different Fourier coefficients as referred in the legend. As in panels (a)-(d) discussed above here the left column [Figs. 7(e) and 7(g)] corresponds to the symmetric and the right one [Figs. 7(f) and 7(h)] to the asymmetric junction. We obtain that these contributions are also constrained by symmetry relations which are

$$A_{n,n}^\uparrow = -B_{n,n}^\uparrow \quad \text{and} \quad A_{n,n}^\downarrow = B_{n,n}^\downarrow. \quad (46)$$

Note that we again plot the absolute values for better comparison. The physical interpretation of these terms is that they correspond to processes where n Cooper pairs are transmitted in one spin band, and zero in the other spin band. For μ pairs transmitted only in the spin- \uparrow band, $A_{\mu,\mu}^\uparrow = (-1)^\mu \mu I_{\mu,0}$, and for ν pairs transmitted only in the spin- \downarrow band, $A_{\nu,\nu}^\downarrow = (-1)^\nu \nu I_{0,\nu}$.

Moreover, we see that in both cases the components exponentially decrease with increasing order n . Comparing the magnitudes of the various terms, we find that

for symmetric junctions a typical hierarchy $|I_{1,0} + I_{0,1}| \gg |I_{1,0} - I_{0,1}| \sim 2I_{1,1} \sim 2I_{1,-1} \sim 2|I_{2,0} + I_{0,2}| \gg 2|I_{2,0} - I_{0,2}|$ is present. For strongly asymmetric junctions, in contrast, $|I_{1,0} + I_{0,1}| \sim 2I_{1,-1} \gg |I_{1,0} - I_{0,1}| \gtrsim 2I_{1,1} \gtrsim 2|I_{2,0} + I_{0,2}| \gg 2|I_{2,0} - I_{0,2}|$ typically holds.

Finally, the $A_{m,n}^\eta$'s and $B_{m,n}^\eta$'s for $m, n > 0$ and $m \neq n$ have a quite small magnitude and we do not discuss them here as they do not give additional insights. However, we find that these contributions also vanish for $(m \pm n)$ odd. The consequence of this finding is, that of all processes where a fixed number of Cooper pairs are transferred across both spin bands, those with equal number of transferred Cooper pairs in the two spin bands dominate over those where in one spin band there are more Cooper pairs transferred than in the other (for example, $|I_{1,1}| > |I_{2,0}|$, $|I_{2,2}| > |I_{3,1}|$, $|I_{4,0}|$ etc). This can be understood in terms of the fact, that when spin-triplet amplitudes are present in the sFM, an equal number of equal-spin Cooper pairs can recombine into spin-singlet pairs on the SC side of the interface without resorting to the triplet rotation mechanism, whereas for any surplus Cooper pairs the triplet rotation mechanism is necessary in order to transform them into singlet Cooper pairs.

In summary, we find that within numerical accuracy our system is described by Eqs. (38)-(40).

D. Analytical model

It follows from Fig. 7 that the lowest harmonic contributions dominate in all cases. We find that a model that includes terms up to second order in the number of transferred Cooper pairs, i.e., $|\mu| + |\nu| \leq 2$, describes the numerical data very closely. Therefore, we write

$$I_{\uparrow\uparrow} \approx I_{1,1} \sin(2\Delta\chi) - I_{1,-1} \sin(2\Delta\varphi) - I_{1,0} \sin(\Delta\chi - \Delta\varphi) + 2I_{2,0} \sin(2\Delta\chi - 2\Delta\varphi), \quad (47)$$

$$I_{\downarrow\downarrow} \approx I_{1,1} \sin(2\Delta\chi) + I_{1,-1} \sin(2\Delta\varphi) - I_{0,1} \sin(\Delta\chi + \Delta\varphi) + 2I_{0,2} \sin(2\Delta\chi + 2\Delta\varphi). \quad (48)$$

This yields the following expressions for $I_{\text{ch}} = I_{\uparrow\uparrow} + I_{\downarrow\downarrow}$ and $I_{\text{sp}} = I_{\uparrow\uparrow} - I_{\downarrow\downarrow}$

$$I_{\text{ch}} \approx 2I_{1,1} \sin(2\Delta\chi) - I_{1+} \sin(\Delta\chi) \cos(\Delta\varphi) + I_{1-} \cos(\Delta\chi) \sin(\Delta\varphi) + I_{2+} \sin(2\Delta\chi) \cos(2\Delta\varphi) - I_{2-} \cos(2\Delta\chi) \sin(2\Delta\varphi), \quad (49)$$

$$I_{\text{sp}} \approx -2I_{1,-1} \sin(2\Delta\varphi) - I_{1-} \sin(\Delta\chi) \cos(\Delta\varphi) + I_{1+} \cos(\Delta\chi) \sin(\Delta\varphi) + I_{2-} \sin(2\Delta\chi) \cos(2\Delta\varphi) - I_{2+} \cos(2\Delta\chi) \sin(2\Delta\varphi), \quad (50)$$

with the definition

$$I_{n\pm} = n(I_{n,0} \pm I_{0,n}). \quad (51)$$

In order to derive analytic expressions for the maximal Josephson diode efficiency, we write $\Delta\varphi = \frac{\pi}{2} + \delta$ and

expand Eqs. (49)-(50) for small δ . Using $\cos(\Delta\varphi) \approx -\delta$, $\sin(\Delta\varphi) \approx 1$, $\cos(2\Delta\varphi) \approx -1$, $\sin(2\Delta\varphi) \approx -2\delta$, this leads to the following model CPR:

$$I_{\text{ch}} \approx 2I_{1,1} \sin(2\Delta\chi) + \delta \cdot I_{1+} \sin(\Delta\chi) + I_{1-} \cos(\Delta\chi) - I_{2+} \sin(2\Delta\chi) + 2\delta \cdot I_{2-} \cos(2\Delta\chi). \quad (52)$$

In our expansion, we will consider I_{2+}/I_{1+} , $I_{1,1}/I_{1+}$, and I_{n-}/I_{n+} to be of the same order of magnitude as δ . This is the case close to the maximal charge Josephson diode efficiency, where δ is small. We then can neglect the term proportional to $\delta \cdot I_{2-}$. We define the two parameters

$$A = 2I_{1,1} - I_{2+}, \quad B = I_{1-}. \quad (53)$$

For $|B| < \sqrt{8}|A|$, the Josephson diode efficiency has maximal magnitude at $\delta = \pm \frac{I_{1-}}{I_{1+}}$, and the model CPR for this value of δ is given by

$$I_{\text{ch}} \approx A \sin(2\Delta\chi) + B [\cos(\Delta\chi) \pm \sin(\Delta\chi)]. \quad (54)$$

This expression has for $|B| < \sqrt{8}|A|$ four extrema. For example, for $\delta = -\frac{I_{1-}}{I_{1+}}$, $A > 0$ they are

$$\Delta\chi_1 = \arctan\left(\frac{S-B}{S+B}\right), \quad I_{\text{ch},1} = A + \frac{B^2}{4A}, \quad (55)$$

$$\Delta\chi_2 = \frac{3}{4}\pi, \quad I_{\text{ch},2} = -A - \sqrt{2}B, \quad (56)$$

$$\Delta\chi_3 = \pi + \arctan\left(\frac{S+B}{S-B}\right), \quad I_{\text{ch},3} = I_c(\Delta\chi_1), \quad (57)$$

$$\Delta\chi_4 = 2\pi - \frac{\pi}{4}, \quad I_{\text{ch},4} = -A + \sqrt{2}B. \quad (58)$$

with $S = \sqrt{8A^2 - B^2}$, and $\Delta\chi_n$ are given modulo 2π . For δ deviating from the optimal value $\pm \frac{I_{1-}}{I_{1+}}$, the degeneracy for the critical currents at $\Delta\chi_1$ and $\Delta\chi_3$ is lifted. The critical currents are $I_{\text{ch}}^+ = A + \frac{B^2}{4A}$, $I_{\text{ch}}^- = -A - \sqrt{2}|B|$. For $A < 0$ a similar consideration gives $I_{\text{ch}}^+ = |A| + \sqrt{2}|B|$, $I_{\text{ch}}^- = -|A| - \frac{B^2}{4|A|}$. The results for $\delta = +\frac{I_{1-}}{I_{1+}}$ are obtained by $\Delta\chi_n \rightarrow -\Delta\chi_n \bmod 2\pi$ and $A \rightarrow -A$, i.e., the same critical currents result with opposite signs. Collecting all together, the charge Josephson diode efficiency with largest magnitude, $\hat{\eta}_{\text{ch}}$, is obtained as

$$\hat{\eta}_{\text{ch}} \approx \pm \frac{4\sqrt{2}|AB| - B^2}{(\sqrt{8}|A| + |B|)^2} \text{sign}(A), \quad (59)$$

where the \pm sign in front of the expression corresponds to $\delta = \pm \frac{I_{1-}}{I_{1+}}$. Comparing this expression with the numerical results of Fig. 5, we obtain from Eq. (59) that $|\hat{\eta}_{\text{ch}}| \approx 26\%$, which is in excellent agreement with the numerical value. Thus, there is excellent agreement. The maximal efficiency that can be obtained from Eq. (59) is for $|B| = \sqrt{2}|A|$ and is 33.3% . The same consideration can be made for $\Delta\varphi$ near $(k + \frac{1}{2})\pi$ with integer k , and the value of $\Delta\varphi$ for optimal efficiency is then given approximately by

$$\widehat{\Delta\varphi}_{\text{ch}} \approx \left(k + \frac{1}{2}\right) \pi \pm \frac{I_{1,0} - I_{0,1}}{I_{1,0} + I_{0,1}} \quad (60)$$

with k integer.

For $|B| > \sqrt{8}|A|$, Eq. (54) exhibits only two extrema. In this case, $I_{\text{ch}}^+ = -A + \sqrt{2}|B|$ and $I_{\text{ch}}^- = -A - \sqrt{2}|B|$. The corresponding values of the Josephson diode efficiency are then

$$\eta_{\text{ch}} \approx \pm \frac{A}{\sqrt{2}|B|}. \quad (61)$$

Here, the maximal efficiency in the range of applicability is attained for $|B| = \sqrt{8}|A|$, for which the values of Eqs. (59) and (61) coincide, and is 25% . However, the optimal value $\hat{\eta}_{\text{ch}}$ is slightly higher than this value, because in this parameter range δ for the optimal efficiency deviates from $\pm \frac{I_{1-}}{I_{1+}}$ (it assumes a smaller magnitude).

It is clear, that these expressions for the charge diode efficiency require A and B to be nonzero for a JDE to occur. As $B = I_{1-}$, this means $I_{1,0} \neq I_{0,1}$. Also, taking into account that $|I_{1,1}| > |I_{2,0}|, |I_{0,2}|$, the condition $I_{1,1} \neq 0$ must be fulfilled. Finally, the JDE is absent for $\delta = 0$, i.e., for $\Delta\varphi = \frac{\pi}{2} + k\pi$ with k integer.

We now turn to the spin current. In particular, we will show, that for certain values of $\Delta\varphi$ the spin current efficiency can reach values of 100% . In general, as long as $\cos(\Delta\varphi)$ does not become too small, the charge current, Eq. (49), is dominated by the term $-I_{1+} \cos(\Delta\varphi) \sin(\Delta\chi)$. The phases for the critical charge currents are then close to $\pm \frac{\pi}{2}$, and given by

$$\Delta\chi_{1/2} \approx \pm \frac{\pi}{2} \pm \frac{4I_{1,1} + 2I_{2+} \cos(2\Delta\varphi) \pm I_{1-} \sin(\Delta\varphi)}{I_{1+} \cos(\Delta\varphi)} \quad (62)$$

and the corresponding spin currents are then

$$I_{\text{sp},1/2} \approx \frac{\mp B - 2 \sin(\Delta\varphi) \{A + C \cos^2(\Delta\varphi)\}}{\cos(\Delta\varphi)} \quad (63)$$

with A and B given in Eq. (53), and

$$C = 2I_{1,-1} + I_{2+}. \quad (64)$$

Equation (63) holds under the condition that $\Delta\chi_{1,2}$ are close to $\pm \frac{\pi}{2}$. The condition, that the spin current vanishes for one of those phases (and therefore a spin diode efficiency of 100% occurs) reads

$$\pm B = -2 \sin(\Delta\varphi) \{A + C \cos^2(\Delta\varphi)\}. \quad (65)$$

For this equation to have a solution, $|B|$ has to be sufficiently small, at least smaller than $\max(2|A|, 4|C|)$. For $|B^2 C| \ll 4|A + C|^3$, we obtain $\hat{\eta}_{\text{sp}} = \pm 1$ for

$$\widehat{\Delta\varphi}_{\text{sp}} \approx k\pi \mp \arcsin\left(\frac{2B}{4(A+C) - B^2 C/(A+C)^2}\right). \quad (66)$$

In this expression, the argument of the arcsin must have a magnitude < 1 . In the limit $|C| \ll |A|$, appropriate for symmetric junctions, this leads to the restriction $|B| <$

$2|A|$. On the other hand, for $|C| \gg |A|$, appropriate for strongly asymmetric junctions, the restriction reads $|B + C| < \sqrt{5}|C|$. For $|C| \gg |A|, |B|$ there is another solution of Eq. (65), which results from a small $\cos^2(\Delta\varphi)$. In this case, also appropriate for strongly asymmetric junctions, a spin diode efficiency of 100% is achieved for (assuming $C > 0$)

$$\widehat{\Delta\varphi}_{\text{sp}} \approx \frac{\pi}{2} + k\pi \pm \arcsin \sqrt{\frac{2(B-2A)}{4C-B}}. \quad (67)$$

under the condition that $B > 2A$. To ensure that the approximations made in Eq. (62) still hold, the condition $|A|, |B| \ll I_{1+} \sqrt{(B-2A)/2C}$ should also apply.

The right hand side of Eq. (65) is a third order polynomial in $\sin(\Delta\varphi)$, which can be solved analytically. The discriminant of this polynomial vanishes at

$$\left(\frac{B}{4C}\right)^2 = \left(\frac{A+C}{3C}\right)^3, \quad (68)$$

indicating that two solutions disappear when $|B/C|$ exceeds some threshold value. In Appendix C we discuss such a case for a strongly asymmetric junction, in which case $|A| \ll |C|$ and the discriminant vanishes for $|B| \approx 4|C|/(3\sqrt{3})$ at a temperature of about $0.22 T_c$. Near this temperature two $\widehat{\Delta\varphi}_{\text{sp}}$ values approach each other, which allows to have a spin-diode efficiency close to 100% in an extended range of $\Delta\varphi$. The value of $\Delta\varphi$ where Eq. (68) is met is given for $2 \geq A/C \geq -1$ by

$$\widehat{\Delta\varphi}_{\text{sp}} = \pm \arcsin \sqrt{\frac{A+C}{3C}}, \quad (69)$$

which for $|C| \gg |A|$ is approximately $\pm \arcsin(1/\sqrt{3})$.

To analyze the above analytical expressions for $\widehat{\eta}_{\text{ch,sp}}$, we perform extensive calculations in Appendix C for homogeneous superconducting order parameters with temperature-dependent BCS gap $\Delta(T)$ (as these calculations are numerically expensive, we do not determine the order parameter profile self-consistently). For each parameter combination we numerically calculate the spin-resolved CPR using the QCGF formalism and obtain spin and charge Josephson diode efficiencies as well as a Fourier decomposition in both $\Delta\chi$ and $\Delta\varphi$. In Fig. 8 we show the maximum values $\eta_{\text{ch,sp}}^{\text{max}} = \max_{\Delta\varphi} |\eta_{\text{ch,sp}}|$, calculated from the Fourier expansion by taking contributions up to $|\mu| + |\nu| \leq 2$, as function of (a) the temperature, (b)+(c) the exchange field strength, and (d) on the transmission probability of the right barrier. In the following, we compare $\eta_{\text{ch,sp}}^{\text{max}}$ with the analytical values $\widehat{\eta}_{\text{ch,sp}}$. First we discuss the functional dependencies shown in panels (a)-(c) of Fig. 8. In agreement with the previous discussion the numerical results show that $\eta_{\text{sp}}^{\text{max}} = 1$ for $|B| \leq 2|A|$. For $|B| > 2|A|$ we obtain that $\eta_{\text{sp}}^{\text{max}}$ monotonically decreases as $B/2A$ increases. Also the numerical results for the maximal charge diode efficiency $\eta_{\text{ch}}^{\text{max}}$ verify the analytic calculations as the maximum magnitude of $\approx 33\%$ is reached for $|B| = \sqrt{2}|A|$ (dashed lines in

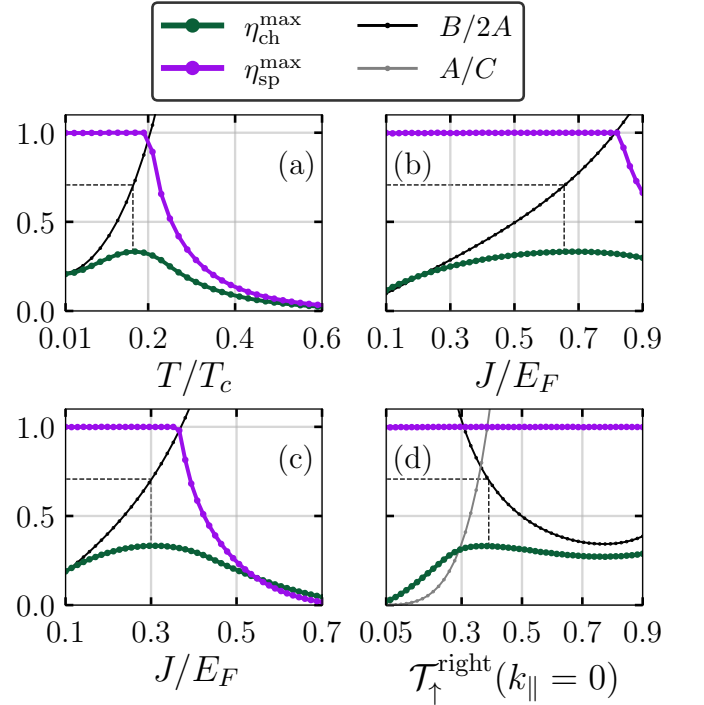


FIG. 8. Functional dependence of maximum diode efficiencies $\eta_{\text{ch,sp}}^{\text{max}}$ and the ratios $B/2A$ and A/C [see Eqs. (53) and (64)] on (a) the temperature, (b) and (c) the exchange field strength for two different Fermi surface geometries [panel (b) has a Fermi surface mismatch as shown in Fig. 2(b) and panel (c) as in Fig. 2(c)], and (d) on the transmission of the right barrier. The corresponding parameter sets are given in the respective Figs. 12-15 of Appendix C.

Fig. 8). We do not show the A/C ratio in panels (a)-(c) of Fig. 8 because $|C| \ll |A|, |B|$ as the considered systems are symmetric. For panel (d) we vary the system from a symmetric junction $\mathcal{T}_{\uparrow}^{\text{right}}(k_{\parallel} = 0) = 0.9$ to a strongly asymmetric one $\mathcal{T}_{\uparrow}^{\text{right}}(k_{\parallel} = 0) = 0.05$. For a high transparency of the right barrier we obtain $|B| < 2|A|$ and $|C| \ll |A|$ and thus Eq. (66) can be used. By decreasing the transparency of the right barrier A decreases whereas C increases. Thus, for $0.3 \leq \mathcal{T}_{\uparrow}^{\text{right}}(k_{\parallel} = 0) \leq 0.4$ we obtain $|A| \sim |C|$ and $\eta_{\text{ch}}^{\text{max}}$ reaches its maximum value as $B/2A$ increases from below $1/\sqrt{2}$ to $B/2A > 1$. From panels (a)-(c) of Fig. 8 we would expect that $\eta_{\text{sp}}^{\text{max}} < 1$ as $|B| > 2|A|$ but in panel (d) $\eta_{\text{sp}}^{\text{max}} = 1$ even for that case. This result follows from Eqs. (66) and (67) as for the strongly asymmetric case $|C| \gg |A|, |B|$ and therefore in the range $B > 2A$ even two solutions with $|\widehat{\eta}_{\text{sp}}| = 1$ exist.

Comparing the results for the two different cases of Fermi surface mismatch shown in Figs. 8(b) and 8(c), it is seen that for panel (b) the maximum charge diode efficiency is reached for $J \approx 0.65E_F$ whereas in the other case the maximum is reached at $J \approx 0.3E_F$. This effect of Fermi surface geometry leads us to an important observation. Scattering processes at the interface can be classified into type-(R): total reflection processes, type-

(H): transmission only into one spin band of the sFM, and type-(F): transmission into both spin bands of the sFM. Scattering processes of type (H), which are of the type which occur at an interface with a half-metallic ferromagnet, appear in our model for $k_F^\downarrow < k_\parallel < \min(k_F^\uparrow, k_F)$. These processes only contribute to $I_{1,0}$, but not to $I_{0,1}$, thus increasing the magnitude of the quantity $I_{1-} = I_{1,0} - I_{0,1}$, which is essential for the Josephson diode effect. Consequently, for given exchange splitting of the electronic bands, the effects are maximized for a Fermi surface geometry of the type shown in Fig. 2(c), for which $k_F^\uparrow \leq k_F$. For a Fermi surface geometry of the type shown in Fig. 2(b), where $k_F^\uparrow \geq k_F$, only the part $k_F^\downarrow < k_\parallel < k_F$ supports type-(H) scattering processes, and the third type of Fermi surface geometry with $k_F^\downarrow > k_F$ (not shown in Fig. 2) has no type-(H) scattering processes at all and therefore exhibits the least pronounced Josephson diode effects. We underline, however, that for Josephson junctions involving purely half-metallic ferromagnets, no Josephson diode effect occurs. Therefore, a trade-off between type-(H) and type-(F) scattering processes takes place, with the former giving important contributions to I_{1-} and the latter to $I_{1,1}$ and $I_{1,-1}$. The highest efficiencies occur when both types of processes contribute to about a similar degree. Thus, the difference between Figs. 8(b) and 8(c) follows from the difference in exchange fields that is needed in order to have a comparable k_\parallel range for which type-(H) scattering events take place.

For a more detailed analysis of Josephson diode efficiencies as functions of temperature, exchange splitting between the bands, and interface transmission asymmetry, we refer to Appendix C.

Next, we discuss the quality of the model CPR in Eqs. (47)-(48) in comparison to numerically obtained CPR's. From Fig. 9(a) follows that by taking into account all contributions shown in Eq. (49) gives a quantitative description of the charge current. Considering only the contributions for $|\mu|, |\nu| \leq 1$ is not sufficient [see Fig. 9(a)] since the $I_{2,0}$ and $I_{0,2}$ contributions are of a comparable order of magnitude [see Figs. 7(a),(e), and (g)]. In contrast, we obtain for the spin current, shown in Fig. 9(b), that for its approximation it is sufficient to account for the contributions where at maximum one Cooper pair is transmitted through each spin-channel. We obtain that the functional dependence on $\Delta\chi$ is dominated by the I_{1+} contribution, i.e., $\cos(\Delta\chi)$. The I_{1-} contribution is comparatively small, but the $I_{1,-1}$ contribution is comparable to the I_{1+} contribution and yields a $\Delta\varphi$ -dependent shift of the CPR.

Finally, we remark that the processes for which an equal number of Cooper pairs is transmitted through each spin channel, i.e., $\mu = \nu$, are the *crossed pair transmission* contributions [12]. The leading term, $I_{1,1}$, dominates the higher harmonics which are crucial for the Josephson diode effect. This term describes a simultaneous transmission of one equal-spin Cooper pair in each spin band. Furthermore, Eq. (50) shows that the spin

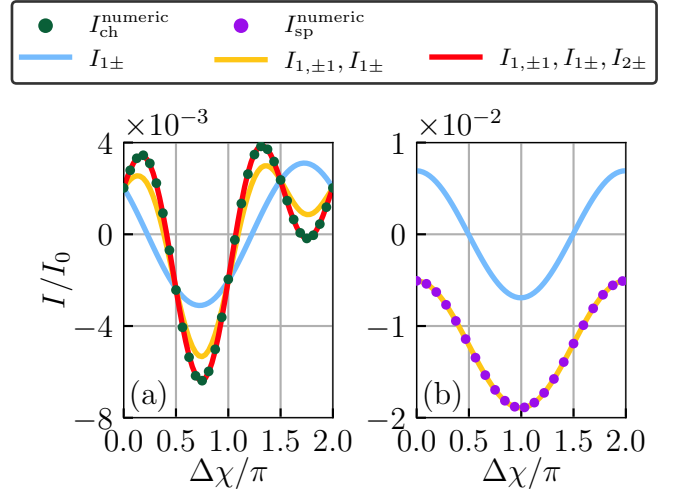


FIG. 9. CPR and its approximations for (a) the charge current in a symmetric junction [see Fig. 5(a)] for $\Delta\varphi = 0.47\pi$, and (b) for the spin current in an asymmetric junction [see Fig. 6(a)] for $\Delta\varphi = \pi/4$. The symbols show the currents numerically obtained from a self-consistent solution (only a few points are shown for a better visibility). The full lines are obtained from the approximations in Eqs. (49)-(50). Different colors take into account different numbers of Fourier contributions as denoted in the legend.

CPR is a superposition between a term constant in $\Delta\chi$ and various oscillating terms. In the case that the magnitude of $2I_{1,-1} \sin(2\Delta\varphi)$ becomes larger than the amplitudes of the oscillating terms (which happens in strongly asymmetric junctions), the spin current flows only in one direction, irrespective of the superconducting phase difference $\Delta\chi$. Were one to define a spin diode efficiency via the maximum and minimum spin currents, then a 100% efficiency would be present for entire ranges of $\Delta\varphi$ in such junctions. However, such a spin current even flows when the Josephson effect is absent, i.e., when one of the two interfaces is intransparent. In this case the charge current is identically zero, such that only terms with $\mu + \nu = 0$ contribute to the Fourier sum in Eqs. (38)-(39). For such a junction, $I_{\text{sp}} = -\sum_{\mu=0}^{\infty} 2\mu I_{\mu,-\mu} \sin(2\mu\Delta\varphi)$ [4, 112]. Therefore, we define the spin Josephson diode effect via the values of the spin current at the phases corresponding to the critical charge currents. In this case, the spin diode efficiency is directly related to the Josephson effect. As we have shown in this article, spin diode efficiency of 100% can still be reached with this definition, namely when for a certain value of $\Delta\varphi$ the spin current vanishes for either $\Delta\chi_{\text{ch}}^+$ or $\Delta\chi_{\text{ch}}^-$.

E. Spontaneous currents

The system carries a spontaneous current even in the absence of a superconducting phase difference at the outer interfaces of the structure. This situation corre-

sponds to a loop geometry with an inserted SC/sFM/SC junction, where the spontaneous current gives rise to a spontaneous flux of $\frac{\Delta\chi_0}{2\pi}\Phi_0$ through the loop [113]. Here, $\Delta\chi_0$ is the phase difference between the two SC/sFM interfaces and Φ_0 is the superconducting flux quantum. The former depends on $\Delta\varphi$ and appears only if $\Delta\varphi \neq k\pi$, $k \in \mathbb{Z}$.

The numerically obtained self-consistent spontaneous charge (green) and spin (violet) currents are shown in Fig. 10. For the symmetric case, both the spontaneous spin and charge current are approximately sinusoidal [see solid lines in Fig. 10]. In contrast, the spontaneous spin current in an asymmetric junction shows a strong second harmonic contribution whereas the charge current is strongly suppressed. This is due to the smaller transparency of the right interface.

We can understand these results in terms of analytical model introduced in Sec. VD. The spontaneous current is obtained from Eqs. (49)-(50) by setting $\Delta\chi = 0$. Neglecting the small terms proportional to $I_{2\pm}$, this leads to

$$I_{\text{ch}}^{\text{spont}} \approx I_{1-} \sin(\Delta\varphi) \quad (70)$$

$$I_{\text{sp}}^{\text{spont}} \approx -2I_{1,-1} \sin(2\Delta\varphi) + I_{1+} \sin(\Delta\varphi). \quad (71)$$

From this it is expected that the spontaneous charge current is approximately sinusoidal in $\Delta\varphi$, whereas the spontaneous spin current is approximately sinusoidal in symmetric junctions, where $I_{1,-1} \ll I_{1+}$, however has pronounced second harmonics in strongly asymmetric junctions, where $I_{1,-1} \sim I_{1+}$. Both spontaneous currents require that $\Delta\varphi$ is not a multiple of π , i.e., they require a *noncoplanar* spin arrangement. The magnitude of the spontaneous charge current is given approximately by $I_{1-} = I_{1,0} - I_{0,1}$, and therefore its presence requires different densities of states in the two spin bands. The magnitude of the spontaneous spin current, on the other hand, is of the order of $I_{1+} = I_{1,0} + I_{0,1}$, and only re-

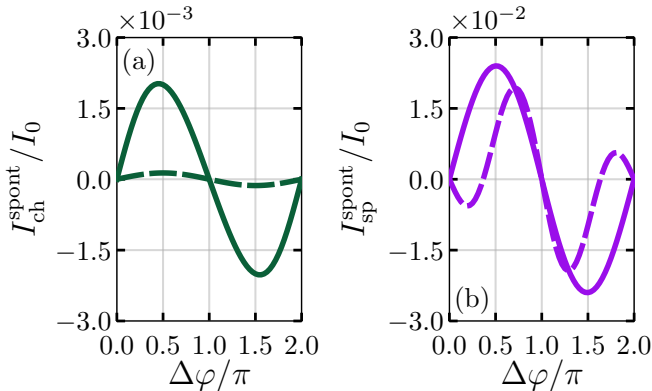


FIG. 10. The functional dependence of (a) the spontaneous charge current and (b) the spontaneous spin current on the geometric phase difference $\Delta\varphi$ for the symmetric system considered in Fig. 5 (solid lines) and the asymmetric system from Fig. 6 (dashed lines), respectively.

quires noncoplanar spin arrangement. The strong second harmonic in $\Delta\varphi$ proportional to $I_{1,-1}$ requires two spin-bands to be present - in a structure with a half-metallic ferromagnet this term is absent.

F. Spin-polarization switch

Finally, we discuss an effect present in both junction types which we consider of being of interest for experimental investigations. Typically, the geometric phase difference $\Delta\varphi$ is fixed during operation of the junction. Therefore, we now consider the systems for fixed $\Delta\varphi$ but varying $\Delta\chi$ which may be realized by embedding the ferromagnetic trilayer considered throughout in a SQUID-geometry and applying a magnetic flux Φ through the loop. Considering the spin-resolved currents for different $\Delta\varphi$'s in Figs. 4(b), 11(a), and 11(d), it becomes evident that there is a value of the superconducting phase difference $\Delta\chi_{\uparrow\uparrow}(\Delta\varphi)$ for which $I_{\uparrow\uparrow}(\Delta\chi_{\uparrow\uparrow}) = 0$ but $I_{\downarrow\downarrow}(\Delta\chi_{\uparrow\uparrow}) \neq 0$. Analogously, there is a value $\Delta\chi_{\downarrow\downarrow}(\Delta\varphi)$ for which $I_{\downarrow\downarrow}(\Delta\chi_{\downarrow\downarrow}) = 0$ but $I_{\uparrow\uparrow}(\Delta\chi_{\downarrow\downarrow}) \neq 0$.

For a quantitative discussion, we define the spin polarization of the current as follows:

$$\mathcal{P}(\Delta\chi) = \frac{|I_{\uparrow\uparrow}(\Delta\chi)| - |I_{\downarrow\downarrow}(\Delta\chi)|}{|I_{\uparrow\uparrow}(\Delta\chi)| + |I_{\downarrow\downarrow}(\Delta\chi)|}. \quad (72)$$

Apparently, for $\Delta\chi = \Delta\chi_{\uparrow\uparrow}$ and $\Delta\chi = \Delta\chi_{\downarrow\downarrow}$ it takes values 1 and -1, respectively, corresponding to a fully spin-polarized current.

As an example let us consider first the spin-resolved currents in a symmetric junction shown in Fig. 11(a). The spin polarization of the Josephson current [see Eq. (72)] for such a situation is presented in panel (b) which displays the characteristic peaks at $\Delta\chi_{\uparrow\uparrow(\downarrow\downarrow)}^{(1,2)}$ as expected from the definition and the index 1,2 denotes the considered branch.

To get a qualitative insight into the switching effects, let us consider the approximate formulas given in the preceding subsection [see Eqs. (47) and (48)] assuming that $|I_{1,-1}|, |I_{2,0}|, |I_{0,2}| < |I_{1,1}| < |I_{0,1}|, |I_{1,0}|$ which is usually the case for symmetric junctions [see Fig. 7]. Thus, the dominating terms for symmetric junctions are of the form

$$I_{\uparrow\uparrow} \approx -I_{1,0} \sin(\Delta\chi - \Delta\varphi) \quad (73)$$

$$I_{\downarrow\downarrow} \approx -I_{0,1} \sin(\Delta\chi + \Delta\varphi). \quad (74)$$

As a result, and as can be seen in Fig. 11(a), the spin-resolved currents for symmetric junctions diminish at $\Delta\chi_{\uparrow\uparrow(\downarrow\downarrow)}^{(1)} \approx \pm\Delta\varphi$ and $\Delta\chi_{\uparrow\uparrow(\downarrow\downarrow)}^{(2)} \approx \pm\Delta\varphi + \pi$. Furthermore, we obtain that the polarization of the current can be switched by changing the superconducting phase difference from $\Delta\chi_{\uparrow\uparrow}^{(1)}$ to $\Delta\chi_{\downarrow\downarrow}^{(1)} \approx -\Delta\chi_{\uparrow\uparrow}^{(1)}$. In a SQUID geometry this transition is equivalent to a reversal of the flux direction, i.e., $\Phi \rightarrow -\Phi$. This effect is interesting for future experimental investigations and may lead potentially to new types of devices. To numerically quantify

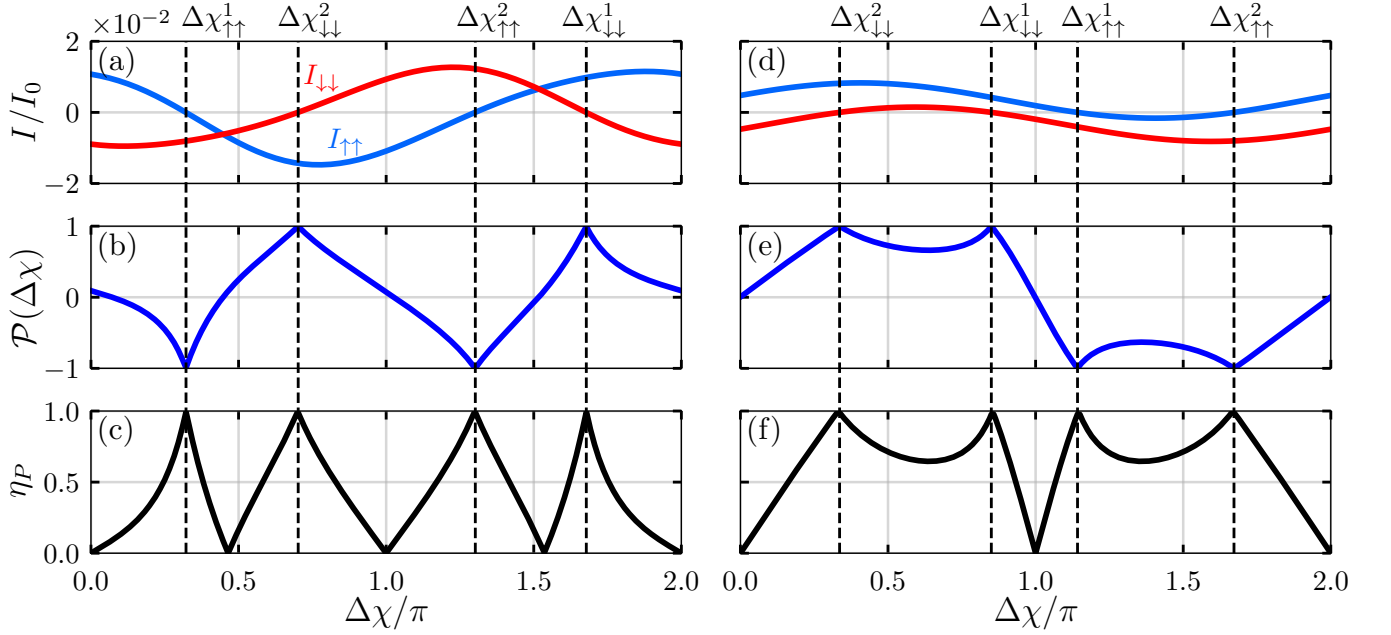


FIG. 11. The functional dependence of the spin-polarization \mathcal{P} [see Eq. (72)] on the superconducting phase difference $\Delta\chi$ for a symmetric junction (b) and an asymmetric junction (e) for the spin-resolved currents shown in (a) and (d), respectively. In (c) and (f) the corresponding switching efficiencies η_P are shown [see Eq.(75)]. For the symmetric case (left column) $\Delta\varphi = 0.31\pi$ and for the asymmetric case (right column) $\Delta\varphi = 0.91\pi$.

the switching effect, we introduce the following quantity:

$$\eta_P(\Delta\chi) = \frac{|P(\Delta\chi) - P(-\Delta\chi)|}{2}, \quad (75)$$

which we term the *switching efficiency*. The functional dependence of $\eta_P(\Delta\chi)$ on the superconducting phase difference $\Delta\chi$ resulting from the CPR in Fig. 11(a) is shown in Fig. 11(c). In contrast to the polarization in Fig. 11(b), the switching efficiency peaks at $\pm(\Delta\chi_{\uparrow\uparrow}^{(1,2)} - \Delta\chi_{\downarrow\downarrow}^{(1,2)})/2$, i.e., slightly besides $\Delta\chi_{\uparrow\uparrow}^{(1,2)}$ and $\Delta\chi_{\downarrow\downarrow}^{(1,2)}$, and reaches up to 99%.

For asymmetric junctions, on the other hand, we have rather $|I_{2,0}|, |I_{0,2}|, |I_{1,1}| < |I_{1,0}|, |I_{0,1}|, |I_{1,-1}|$, and therefore the dominating terms in Eqs. (47) and (48) are

$$I_{\uparrow\uparrow} \approx -I_{1,0} \sin(\Delta\chi - \Delta\varphi) - I_{1,-1} \sin(2\Delta\varphi) \quad (76)$$

$$I_{\downarrow\downarrow} \approx -I_{0,1} \sin(\Delta\chi + \Delta\varphi) + I_{1,-1} \sin(2\Delta\varphi). \quad (77)$$

Thus, both have an additional constant term (independent of $\Delta\chi$), which for $\Delta\varphi \neq k\pi/2$ shifts the CPRs in vertical direction, modifying the zero crossings. As a consequence, we obtain a switching effect for asymmetric junctions as shown in Figs. 11(e) and 11(f); although qualitatively similar to the case of symmetric junctions, quantitatively the functional dependencies are different and three cases can be distinguished. Firstly, for certain $\Delta\varphi$ we obtain the same effect as discussed for the symmetric junction, i.e., \mathcal{P} and η_P peak at $\Delta\chi_{\uparrow\uparrow(\downarrow\downarrow)}^{(1/2)}$ and reach zero between two peaks. Secondly, if $\Delta\varphi$ is chosen such that neither $I_{\uparrow\uparrow}$ nor $I_{\downarrow\downarrow}$ change their sign as function of $\Delta\chi$, \mathcal{P} does not reach ± 1 and consequently $\eta_P < 1$

for all $\Delta\chi$. Finally, when $I_{\uparrow\uparrow}$ and $I_{\downarrow\downarrow}$ do not intersect, i.e., $I_{\uparrow\uparrow} \neq I_{\downarrow\downarrow}$ for all $\Delta\chi$ [see Fig. 11(d)], we obtain that $\mathcal{P} = \pm 1$ and $\eta_P \approx 99\%$ at $\Delta\chi_{\uparrow\uparrow(\downarrow\downarrow)}^{(1/2)}$ but the polarization and the switching efficiency only vanish for $\Delta\chi = k\pi$, $k \in \mathbb{Z}$. Thus, for $\Delta\chi \in [\Delta\chi_{\uparrow\uparrow}^{(1/2)}, \Delta\chi_{\downarrow\downarrow}^{(1/2)}]$ the polarization \mathcal{P} and η_P remain at comparatively high values. Consequently, the superconducting phase difference, and thus the flux Φ , do not need to be adjusted too accurately to $\Delta\chi_{\uparrow\uparrow(\downarrow\downarrow)}^{(1/2)}$ to achieve a highly spin-polarized current and a high switching efficiency. Hence, even though the currents are smaller in the asymmetric junction, it might be easier to exploit this effect in applications.

VI. CONCLUSION

In summary, we have presented a systematic theoretical analysis of the Josephson diode effect in macroscopic hybrid junctions comprising a strongly spin-polarized ferromagnet sandwiched between two BCS superconducting leads via two spin-active insulating interfaces. The study has been delivered in the framework of modified quasiclassical Green's function formalism in the diffusive limit adapted to strongly spin-polarized weak links. Namely, a strong exchange field in the sFM allows neglecting the mixed-spin correlations (spin singlets and spin triplets with $s_z = 0$) ending up with the equal-spin triplets ($s_z = \pm 1$). This regime allows us to get an insight in spin-resolved quantities and accordingly calculate the

transport properties.

We have focussed on the role of the relative azimuthal angle between the magnetizations of the two ferromagnetic interfaces, which plays the role of a *quantum-geometric phase difference*, $\Delta\varphi$, by entering directly the Josephson current phase relation. We have shown that the Josephson diode effect can be realized if the following conditions are fulfilled: (i) noncoplanar spin texture, i.e., nonvanishing $\Delta\varphi$ (but $\Delta\varphi \neq k\pi/2$) and (ii) different densities of states between the spin bands (i.e., Fermi surface spin splitting). Both spin bands are required in order to enable prominent crossed pair transmission processes, i.e., the effects are absent in half-metals. The mentioned requirements are fulfilled in the case of a strongly spin-polarized ferromagnet and a noncoplanar profile of magnetizations in the trilayer. A strong spin polarization of the central region destroys any coherence of pair correlations that involve both spin bands, allowing only equal-spin pairs amplitudes to enter either spin- \uparrow or spin- \downarrow bands. Our model predicts charge diode efficiency up to $\eta_{\text{ch}} \gtrsim 33\%$ and a perfect spin diode effect with $\eta_{\text{sp}} = 100\%$ in symmetric junctions.

To get more insight into the role of the geometric phases, we have performed the harmonic analysis of the spin-resolved currents both in $\Delta\chi$ and $\Delta\varphi$, where the former denotes the superconducting phase difference. We discussed symmetries between the Fourier coefficients and derived a physically appealing model in which $\Delta\chi$ and $\Delta\varphi$ enter the theory on equal footing.

Beside the diode effects, we have analyzed the spin switching effects in the system. We have shown that the SQUID geometry involving a ferromagnetic trilayer can feature fully spin-polarized supercurrents. In addition, we have shown that its polarization can be well controlled by an external magnetic flux.

Finally, our model can serve as a platform for further experimental investigations of the Josephson charge and spin diode effect in mesoscopic hybrids involving strongly spin-polarized ferromagnets. In addition, the discussed system can be a promising platform for experimental investigation of spin switching effects in SQUID devices involving ferromagnetic trilayers.

ACKNOWLEDGMENTS

We thank Ralf Schneider for fruitful discussions. NLS and ME acknowledge funding by the Deutsche Forschungsgemeinschaft (DFG, German Research Foundation) under project number 530670387. The computations were enabled by resources provided by the University Computer Centre of the University of Greifswald.

Appendix A: Calculation of the Fourier coefficients

As shown in the the main text, noncoplanar spin textures in SC/sFM/SC trilayers introduce the geometric

phase difference $\Delta\varphi$, which enters the current-phase relations. Therefore, a Fourier decomposition of the spin-resolved currents both in the superconducting phase difference $\Delta\chi = \chi_2 - \chi_1$ and the geometric phase difference $\Delta\varphi = \varphi_2 - \varphi_1$ can be performed to gain more insights.

Starting from the Fourier expansion Eq. (42) we obtain

$$I_{\eta\eta}(\Delta\chi, \Delta\varphi) = \frac{1}{4} \sum_{m,n=-\infty}^{\infty} A_{m,n}^{\eta} \sin(m\Delta\chi) \cos(n\Delta\varphi) + B_{m,n}^{\eta} \cos(m\Delta\chi) \sin(n\Delta\varphi), \quad (\text{A1})$$

where we formally extended the Fourier sums over n and m to $-\infty$ using the definitions

$$A_{-m,n}^{\eta} = -A_{m,n}^{\eta}, \quad A_{m,-n}^{\eta} = A_{m,n}^{\eta}, \quad (\text{A2})$$

$$B_{-m,n}^{\eta} = B_{m,n}^{\eta}, \quad B_{m,-n}^{\eta} = -B_{m,n}^{\eta}. \quad (\text{A3})$$

In particular, it follows that $A_{0,n}^{\eta} = 0$, $B_{m,0}^{\eta} = 0$. Eq. (A1) can be rewritten using the trigonometric identity $\sin\alpha \cos\beta = \frac{1}{2} [\sin(\alpha + \beta) + \sin(\alpha - \beta)]$, as

$$I_{\eta\eta} = \frac{1}{4} \sum_{m,n=-\infty}^{\infty} (A_{m,n}^{\eta} + B_{m,n}^{\eta}) \sin(m\Delta\chi + n\Delta\varphi) + (A_{m,n}^{\eta} - B_{m,n}^{\eta}) \sin(m\Delta\chi - n\Delta\varphi). \quad (\text{A4})$$

Renaming the summation variable n in the first line into $-n$ and using Eqs. (A2)-(A3) leads with the definition $\mathcal{J}_{m,n}^{\eta} = (A_{m,n}^{\eta} - B_{m,n}^{\eta})/2$ to

$$I_{\eta\eta}(\Delta\chi, \Delta\varphi) = \frac{1}{2} \sum_{m,n=-\infty}^{\infty} \mathcal{J}_{m,n}^{\eta} \sin(m\Delta\chi - n\Delta\varphi), \quad (\text{A5})$$

where $\mathcal{J}_{m,n}^{\eta} = -\mathcal{J}_{-m,-n}^{\eta}$. The numerical current-phase relations allow for the calculation of the Fourier components $A_{m,n}^{\eta}$ and $B_{m,n}^{\eta}$ which are shown for the case of a symmetric and a asymmetric junction configuration in Fig. 7. Explicit numerical evaluation confirms that the Fourier components are restrained by additional symmetry relations, some of which are summarized in Table A, and which can be summarized by the relation

$$n (\mathcal{J}_{m,n}^{\uparrow} + \mathcal{J}_{m,n}^{\downarrow}) = m (\mathcal{J}_{m,n}^{\uparrow} - \mathcal{J}_{m,n}^{\downarrow}). \quad (\text{A6})$$

Our analysis leads to nonzero Fourier coefficients only for combinations of m and n where $m \pm n$ are even integers. We therefore pass to new integer indices (μ, ν) defined as $\mu = (m + n)/2$ and $\nu = (m - n)/2$. Accordingly, we define $I_{\mu,\nu}^{\eta} \equiv \mathcal{J}_{\mu+\nu,\mu-\nu}^{\eta}$. Consequently, the corresponding symmetry relations are shown in the right column of Table A and the above relation for $\mathcal{J}_{m,n}^{\eta}$ reads

$$(\mu - \nu) (I_{\mu,\nu}^{\uparrow} + I_{\mu,\nu}^{\downarrow}) = (\mu + \nu) (I_{\mu,\nu}^{\uparrow} - I_{\mu,\nu}^{\downarrow}), \quad (\text{A7})$$

or, equivalently,

$$\mu I_{\mu,\nu}^{\downarrow} = \nu I_{\mu,\nu}^{\uparrow}. \quad (\text{A8})$$

TABLE I. Tabulated symmetries between $A_{m,n}^\eta$ and $B_{m,n}^\eta$ coefficients [see Eq. (A1)], for the $\mathcal{J}_{m,n}^\eta$ coefficients [see Eq. (A5)], and the $I_{\mu,\nu}^\eta$'s.

Symmetries in		
$A_{m,n}^\eta$ and $B_{m,n}^\eta$	$\mathcal{J}_{m,n}^\eta$	$I_{\mu,\nu}^\eta$
$A_{m,0}^\uparrow = A_{m,0}^\downarrow$	$\mathcal{J}_{m,0}^\uparrow = \mathcal{J}_{m,0}^\downarrow$	$I_{\mu,\mu}^\uparrow = I_{\mu,\mu}^\downarrow$
$B_{0,n}^\uparrow = -B_{0,n}^\downarrow$	$\mathcal{J}_{0,n}^\uparrow = -\mathcal{J}_{0,n}^\downarrow$	$I_{\mu,-\mu}^\uparrow = -I_{\mu,-\mu}^\downarrow$
$A_{m,m}^\uparrow = -B_{m,m}^\uparrow$	$\mathcal{J}_{m,-m}^\uparrow = 0$	$I_{0,\nu}^\uparrow = 0$
$A_{m,m}^\downarrow = B_{m,m}^\downarrow$	$\mathcal{J}_{m,m}^\downarrow = 0$	$I_{\mu,0}^\downarrow = 0$

Defining $I_{\mu,\nu}^\uparrow = \mu \tilde{I}_{\mu,\nu}$, this leads to

$$I_{\mu,\nu}^\uparrow = \mu \cdot \tilde{I}_{\mu,\nu} \quad \text{and} \quad I_{\mu,\nu}^\downarrow = \nu \cdot \tilde{I}_{\mu,\nu}, \quad (\text{A9})$$

where $\tilde{I}_{-\mu,-\nu} = \tilde{I}_{\mu,\nu}$. This allows to rewrite the initial Fourier ansatz, see Eq. (A1), as

$$\begin{aligned} I_{\uparrow\uparrow} &= \frac{1}{2} \sum_{\mu,\nu=-\infty}^{\infty} \mu \tilde{I}_{\mu,\nu} \sin[(\mu + \nu)\Delta\chi - (\mu - \nu)\Delta\varphi], \\ I_{\downarrow\downarrow} &= \frac{1}{2} \sum_{\mu,\nu=-\infty}^{\infty} \nu \tilde{I}_{\mu,\nu} \sin[(\mu + \nu)\Delta\chi - (\mu - \nu)\Delta\varphi], \end{aligned} \quad (\text{A10})$$

which are Eqs. (38) and (39) from the main text, where we wrote $\tilde{I}_{\mu,\nu} = (-1)^{\mu+\nu} I_{\mu,\nu}$.

Appendix B: Boundary conditions for the coherence amplitudes

The normalization of the quasiclassical Green's function allows to express it in terms of projectors \hat{P}_\pm [83, 108]

$$\hat{G} = (\hat{P}_+ - \hat{P}_-), \quad (\text{B1})$$

where \hat{P}_\pm is defined as

$$\hat{P}_\pm = \frac{1}{2} (\hat{1} \pm \hat{G}). \quad (\text{B2})$$

It can be easily shown that these are projectors having the following properties:

$$\hat{P}_\pm^2 = \hat{P}_\pm, \quad (\text{B3a})$$

$$\hat{P}_+ \hat{P}_- = \hat{P}_- \hat{P}_+ = \hat{0}, \quad (\text{B3b})$$

$$\hat{P}_+ + \hat{P}_- = \hat{1}, \quad (\text{B3c})$$

implying

$$\frac{\partial \hat{P}_+}{\partial z} = -\frac{\partial \hat{P}_-}{\partial z}, \quad (\text{B4})$$

$$\frac{\partial \hat{P}_\pm}{\partial z} \hat{P}_\mp = -\hat{P}_\pm \frac{\partial \hat{P}_\mp}{\partial z}, \quad (\text{B5})$$

$$\hat{P}_\pm \frac{\partial \hat{P}_\mp}{\partial z} \hat{P}_\pm = \hat{0}. \quad (\text{B6})$$

Using the above expression, the following identity can be easily derived

$$\begin{aligned} \frac{\partial \hat{P}_+}{\partial z} &= (\hat{P}_+ + \hat{P}_-) \frac{\partial \hat{P}_+}{\partial z} (\hat{P}_+ + \hat{P}_-) \\ &= \hat{P}_+ \frac{\partial \hat{P}_+}{\partial z} \hat{P}_- + \hat{P}_- \frac{\partial \hat{P}_+}{\partial z} \hat{P}_+. \end{aligned} \quad (\text{B7})$$

An analogous expression can be derived for \hat{P}_- by exchanging + and - indices in the above equation.

The boundary condition for the Green's function Eq. (32) can be written in terms of projectors as

$$\frac{\partial \hat{P}_+}{\partial z} - \frac{\partial \hat{P}_-}{\partial z} = 2 \frac{\partial \hat{P}_+}{\partial z} = -\frac{1}{r} (\hat{P}_+ - \hat{P}_-) \hat{\mathcal{I}}, \quad (\text{B8})$$

which by multiplying from the left with \hat{P}_+ and using Eqs. (B7), (B3a) and (B3b) is rewritten as

$$\hat{P}_+ \frac{\partial \hat{P}_+}{\partial z} \hat{P}_- = -\frac{1}{2r} \hat{P}_+ \hat{\mathcal{I}}. \quad (\text{B9})$$

An analogous calculation leads to

$$\hat{P}_- \frac{\partial \hat{P}_-}{\partial z} \hat{P}_+ = -\frac{1}{2r} \hat{P}_- \hat{\mathcal{I}}. \quad (\text{B10})$$

Multiplying Eq. (B9) from the right with \hat{P}_+ and Eq. (B10) from the right with \hat{P}_- yields

$$\hat{P}_\pm \hat{\mathcal{I}} \hat{P}_\pm = \hat{0}. \quad (\text{B11})$$

Since we use coherence (Riccati) amplitudes in this work, we express the above relation in its terms. We start from projectors that read as follows [83]:

$$\hat{P}_+ = \begin{pmatrix} 1 \\ -\tilde{\gamma} \end{pmatrix} N(1, \gamma), \quad (\text{B12})$$

$$\hat{P}_- = \begin{pmatrix} -\gamma \\ 1 \end{pmatrix} \tilde{N}(\tilde{\gamma}, 1), \quad (\text{B13})$$

$$N = (1 - \gamma\tilde{\gamma})^{-1}, \quad \tilde{N} = (1 - \tilde{\gamma}\gamma)^{-1}, \quad (\text{B14})$$

Eq. (B11) then takes the form

$$\bar{\mathcal{I}}_{11} + \gamma \bar{\mathcal{I}}_{21} - \bar{\mathcal{I}}_{12} \tilde{\gamma} - \gamma \bar{\mathcal{I}}_{22} \tilde{\gamma} = 0, \quad (\text{B15})$$

$$\bar{\mathcal{I}}_{22} + \tilde{\gamma} \bar{\mathcal{I}}_{12} - \bar{\mathcal{I}}_{21} \gamma - \tilde{\gamma} \bar{\mathcal{I}}_{11} \gamma = 0. \quad (\text{B16})$$

The left hand side of Eq. (B9) adopts the form

$$\hat{P}_+ \frac{\partial \hat{P}_+}{\partial z} \hat{P}_- = \begin{pmatrix} 1 \\ -\tilde{\gamma} \end{pmatrix} N \frac{\partial \gamma}{\partial z} \tilde{N}(\tilde{\gamma}, 1). \quad (\text{B17})$$

Similarly the $\hat{P}_+ \hat{\mathcal{I}}$ term on the right hand side of the same equation can be evaluated, finally, leading to the boundary conditions

$$\begin{pmatrix} N \frac{\partial \tilde{\gamma}}{\partial z} \tilde{N} \tilde{\gamma} & N \frac{\partial \tilde{\gamma}}{\partial z} \tilde{N} \\ -\tilde{\gamma} N \frac{\partial \tilde{\gamma}}{\partial z} \tilde{N} \tilde{\gamma} & -\tilde{\gamma} N \frac{\partial \tilde{\gamma}}{\partial z} \tilde{N} \end{pmatrix} = -\frac{1}{2r} \begin{pmatrix} N \bar{\mathcal{I}}_{11} + N \gamma \bar{\mathcal{I}}_{21} & N \bar{\mathcal{I}}_{12} + N \gamma \bar{\mathcal{I}}_{22} \\ -\tilde{\gamma} N \bar{\mathcal{I}}_{11} - \tilde{\gamma} N \gamma \bar{\mathcal{I}}_{21} & -\tilde{\gamma} N \bar{\mathcal{I}}_{12} - \tilde{\gamma} N \gamma \bar{\mathcal{I}}_{22} \end{pmatrix}, \quad (\text{B18})$$

Note that in the above equation the various matrix components are not independent, and only one condition follows from them. Since we are free to choose one equation, we take the (12)-component of the above equation and rewrite it as follows:

$$-2r \frac{\partial \tilde{\gamma}}{\partial z} = (\bar{\mathcal{I}}_{12} + \gamma \bar{\mathcal{I}}_{22}) \tilde{N}^{-1}. \quad (\text{B19})$$

A boundary condition for $\partial \tilde{\gamma} / \partial z$ is obtained by considering \hat{P}_- instead of \hat{P}_+ in Eq. (34) which results in

$$-2r \frac{\partial \tilde{\gamma}}{\partial z} = (\bar{\mathcal{I}}_{21} + \tilde{\gamma} \bar{\mathcal{I}}_{11}) N^{-1}. \quad (\text{B20})$$

These boundary conditions differ from, but can be shown to be equivalent to those derived in Ref. [107].

Appendix C: Functional dependence of diode efficiency and spontaneous currents on the system parameters

In the main text we have concentrated on discussing the Josephson diode efficiency on the geometric phase difference $\Delta\varphi$. In this Appendix we discuss the Josephson diode efficiencies as function of additional system parameters such as temperature, exchange splitting of the electronic bands in the ferromagnet, or transmission probability asymmetry between the left and right interfaces of the ferromagnet. As the numerical calculations are very extensive, we consider for the following numerical results homogeneous superconductors (no spatial variation of the order parameter) to each side of the strongly spin-polarized ferromagnet. The homogeneous superconductors are characterized by a temperature dependent BCS gap $\Delta(T)$. We first discuss charge and spin diode efficiencies and proceed afterwards to spontaneous currents in a loop geometry.

1. Diode Efficiencies

We first consider a symmetric junction whose parameters are the same as in Fig. 5 but in which both spin-channels have the same barrier width of $0.6\lambda_F/2\pi$. We then vary the temperature that leads to a variation of the superconducting order parameter $\Delta(T)$ with temperature. Fig. 12 shows the charge [panel (a)] and the spin diode efficiency [panel (b)] as a function the geometric phase $\Delta\varphi$ and the temperature T . We obtain that for lower temperatures up to $T \approx 0.2T_c$ there is a significant diode effect in both, the charge and the spin current. Moreover, η_{ch} increases reaching its maximum around $T \approx 0.2T_c$. On the other hand, $\Delta\varphi$ at which

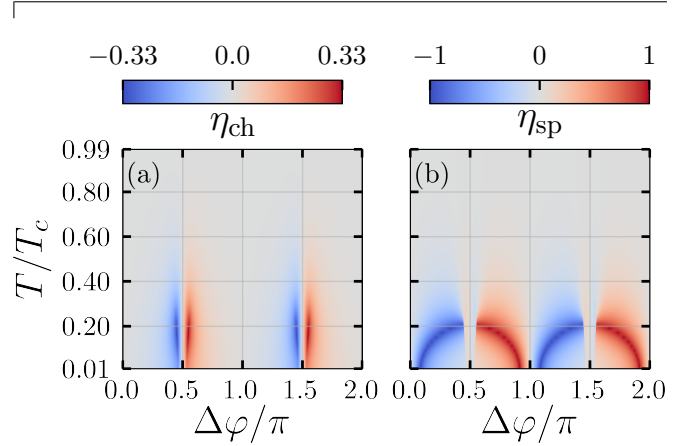


FIG. 12. The functional dependence of the charge [panel (a)] and spin [panel (b)] diode efficiencies $\eta_{\text{ch/sp}}$ on the geometric phase $\Delta\varphi$ and the temperature T of a symmetric Josephson junction. Note that the superconducting order parameter $\Delta(T)$ also varies with temperature. The remaining parameters are as in Fig. 4 except that the barriers on the left and right side have now the same width for both spin-channels which is $0.6\lambda_F/2\pi$. As in the main text the diode efficiencies are calculated by using the Fourier expansion of the currents [see Eqs. (38) and (39)] for which the numerically obtained Fourier contributions were utilised.

$\eta_{\text{sp}} = \pm 1$, i.e., $\widehat{\Delta\varphi}_{\text{sp}}$ [see Sec. VD], shifts from $k\pi$ towards $(k + \frac{1}{2})\pi$ as T approaches $0.2T_c$. This shift can be understood by considering the approximations in section VD and Fig. 8(a) where we show the $B/2A$ ratio for the results shown here in Fig. 12. From Eq. (66) follows for $|C| \ll |A|, |B|$, which is the case here, that $\widehat{\Delta\varphi}_{\text{sp}} \approx \mp \arcsin(B/2A)$. Thus, for low temperatures where $B < 2A$ we get $\widehat{\Delta\varphi}_{\text{sp}} \approx 0$ and as $B/2A$ increases $\widehat{\Delta\varphi}_{\text{sp}} \rightarrow \pi/2$. If $B > 2A$, then there exists no $\Delta\varphi$ which solves Eq. (65) and thus $\eta_{\text{sp}}^{\text{max}}$ decreases for $B/2A > 1$, i.e., for temperatures exceeding $T \approx 0.2T_c$.

Another parameter which appears to be important for the effect is the exchange field strength in the barriers and the ferromagnet which are here, for definiteness, assumed to be equal ($J_B = J_{\text{sFM}} = J$). To study the effect of varying exchange field strength, in what follows we set the temperature to $T = 0.1T_c$ and vary the exchange field within the range $0.1 < J/E_F < 0.9$. Moreover, we for now consider the case in which $V_{\text{sFM}} = 0$, i.e., $V_{\text{sFM}}^{\uparrow(\downarrow)} = \mp J/2$ and $k_F^\downarrow < k_F < k_F^\uparrow$, and V_B^\uparrow is fixed to $V_B^\uparrow = 1.1E_F$ and therefore $V_B^\downarrow = V_B^\uparrow + J$. Figure 13 shows η_{ch} [panel (a)] and η_{sp} [panel (b)] as functions of $\Delta\varphi$ and J . Apparently, the diode effect is present for all considered exchange field strengths but the functional dependencies and the magnitudes are affected by varying J . The functional dependence of the charge diode efficiency

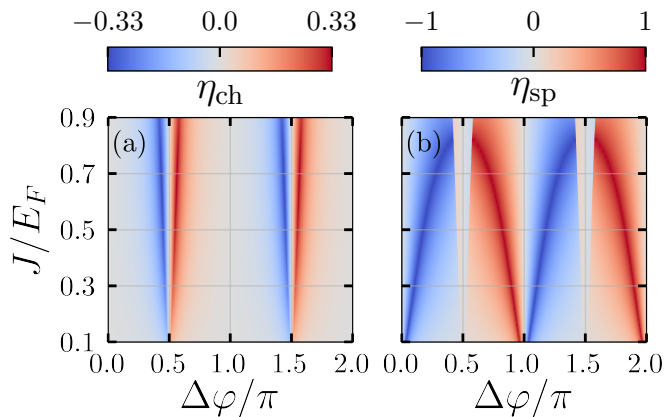


FIG. 13. The functional dependence of the charge [panel (a)] and spin [panel (b)] diode efficiencies $\eta_{\text{ch/sp}}$ of a symmetric Josephson junction on the geometric phase $\Delta\varphi$ and the exchange field strength J which is assumed to be the same in the barriers and the sFM. In the sFM no bias potential is applied, i.e. $V_{\text{sFM}} = 0$, whereas in the barrier $V_{\text{B}}^{\uparrow} = 1.1E_F$ and thus $V_{\text{B}}^{\downarrow} = V_{\text{B}}^{\uparrow} + J$. The left and right barrier are for both spin-channels $0.6\lambda_F/2\pi$ wide, the length of the sFM is ξ and the temperature is $T = 0.1T_c$.

is unaffected by the exchange field strength but its magnitude increases with increasing exchange field strength until the maximum is reached around $J \approx 0.7E_F$ and starts to decrease for further increment of the exchange field strength. This effect is not visible in the picture due to the colormap. In contrast, we obtain that the functional dependence of $\eta_{\text{sp}}(\Delta\varphi)$ is significantly affected as the maxima and minima shift from $k\pi$ towards $(k + \frac{1}{2})\pi$. This shift can be reasoned in the same way as done for the temperature dependence and the corresponding $B/2A$ ratio and $\eta_{\text{ch,sp}}^{\text{max}}$ are shown in Fig. 8(b). Furthermore, when $B > 2A$, i.e., $J \gtrsim 0.8E_F$, we also obtain that $\eta_{\text{sp}}^{\text{max}} < 1$ in agreement with Eq. (65).

In addition to the case for which $V_{\text{sFM}} = 0$ we have studied the case in which V_{sFM} is J -dependent such that $V_{\text{sFM}}^{\uparrow}$ is fixed to $V_{\text{sFM}}^{\uparrow} = 0.1E_F$ but $V_{\text{sFM}}^{\downarrow}$ varies with the exchange field $V_{\text{sFM}}^{\downarrow} = V_{\text{sFM}}^{\uparrow} + J$. In this case the barrier potentials are given by $V_{\text{B}}^{\uparrow(\downarrow)} = V_{\text{sFM}}^{\uparrow(\downarrow)} + E_F$. The functional dependencies, shown in Fig. 14, differ from Fig. 13 and we obtain a similar effect as obtained for the previous case for which the same reasoning applies. Only the exact exchange fields, at which the maximum magnitude of the charge diode effect and the exchange field at which the perfect spin diode effect vanishes, differ. Moreover, the maximum diode efficiencies quickly decrease towards zero for larger exchange fields. This is because the \downarrow -band is then close to the Fermi level and if the band becomes insulating, i.e., $J > 0.9E_F$, the strongly spin-polarized ferromagnet becomes a half-metal. In the half-metallic case all contributions in which the \downarrow -band is involved vanish, i.e., $I_{\mu,\nu} = 0$ for $\nu \neq 0$. Therefore, in the half-metallic case $I_{\text{ch,sp}} = I_{\uparrow\uparrow} = \sum_{\mu=1}^{\infty} \mu(-1)^{\mu} I_{\mu,0} \sin[\mu(\Delta\chi - \Delta\varphi)]$ and thus the diode effect is absent as positive and nega-

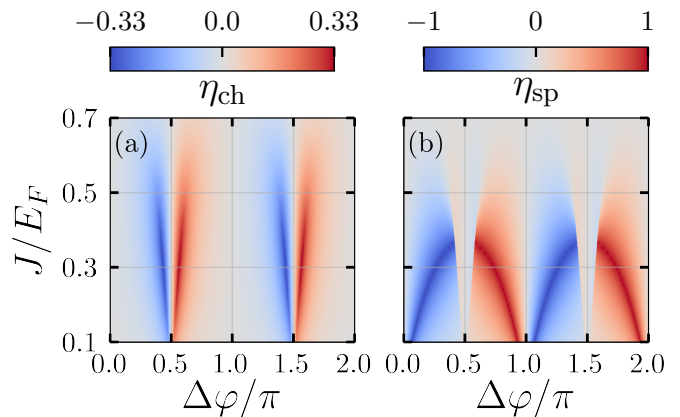


FIG. 14. The functional dependence of the charge [panel (a)] and the spin [panel (b)] diode efficiencies $\eta_{\text{ch/sp}}$ of a symmetric Josephson junction on the geometric phase $\Delta\varphi$ and the exchange field strength J . Here the \uparrow -band in the sFM is fixed to $V_{\text{sFM}}^{\uparrow} = 0.1E_F$ and the \downarrow -band is shifted by J , i.e., $V_{\text{sFM}}^{\downarrow} = V_{\text{sFM}}^{\uparrow} + J$. The barrier potentials are then given by $V_{\text{B}}^{\uparrow(\downarrow)} = E_F + V_{\text{sFM}}^{\uparrow(\downarrow)}$. The remaining parameters are the same as for Fig. 13.

tive critical current are always of the same magnitude in that case.

Finally, we consider in Fig. 15 the effect of the barrier width d which allows to look at the crossover between a symmetric junction to an asymmetric one. To see the effect, we consider the diode efficiencies as functions of the right barrier's widths whereas the left one is fixed at $0.6\lambda_F/2\pi$ corresponding to the transmission for perpendicular impact ($k_{\parallel} = 0$) of $\mathcal{T}_{\uparrow}^{\text{left}} \approx 0.9$. Intuitively, it is clear that d is related to the transmission probability of particles through the barrier therefore we focus here on the latter.

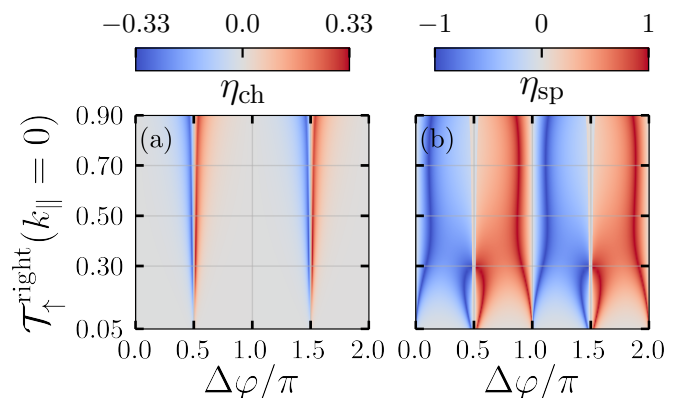


FIG. 15. The functional dependence of the charge [panel (a)] and spin [panel (b)] diode efficiencies $\eta_{\text{ch/sp}}$ on the geometric phase difference $\Delta\varphi$ and the transmission of the right barrier characterised by the transmission $\mathcal{T}_{\uparrow}^{\text{right}}(k_{\parallel} = 0)$, with $\mathcal{T}_{\uparrow}^{\text{left}}(k_{\parallel} = 0)$ fixed at 0.9. The potentials and exchange fields are as for Fig. 5 just the spin-resolved barrier widths of the left barrier are now both $0.6\lambda_F/2\pi$ wide.

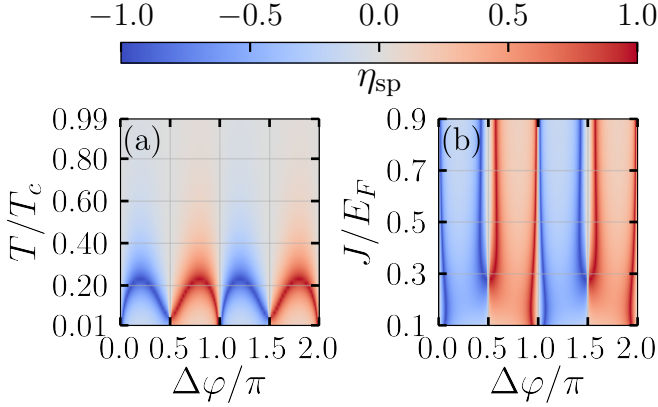


FIG. 16. Functional dependence of the spin diode efficiency η_{sp} on the geometric phase $\Delta\varphi$ for varying temperature (a) and exchange field strength (b) [Fermi surface mismatch as shown in Fig. 2(b)]. For both panels the barriers of the two spin-channels are of the same width for each side. The left barrier is $0.6\lambda_F/2\pi$ wide and the right barrier is $3.1\lambda_F/2\pi$ wide, i.e., $\mathcal{T}_{\uparrow}^{\text{left}}(k_{\parallel} = 0) = 0.9$ and $\mathcal{T}_{\uparrow}^{\text{right}}(k_{\parallel} = 0) = 0.2$. For panel (a) the exchange fields and potentials are as for Fig. 12 and for panel (b) the temperature is $T = 0.1T_c$.

Fig. 15 shows the charge [panel (a)] and the spin [panel (b)] diode efficiency as a function of the geometric phase difference $\Delta\varphi$ and the spin-up transmission coefficient of the right barrier. For a more detailed analysis we consider the analytic model from Sec. VD. The maximum charge diode efficiency is reached at $B = \sqrt{2}A$ and the functional dependence is unaffected by changing the transmission of the right barrier. In contrast, the functional dependence of the spin diode efficiency is strongly altered as it peaks at both $k\pi$ and $(k + \frac{1}{2})\pi$ for $\mathcal{T}_{\uparrow}^{\text{right}}(k_{\parallel} = 0) \leq 0.38$ and only at $k\pi$ for a more transparent barrier. The additional peaks follow from Eq. (65) which in the considered case has a solution close to $k\pi$ [see Eq. (66)] and another solution close to $(k + \frac{1}{2})\pi$ [see Eq. (67)].

In Fig. 16 we consider the spin diode efficiency in the case of an asymmetric junction where the left barrier is of high transparency and the right barrier is less transparent but not in the tunneling limit. We obtain that perfect efficiency also is absent for $T \gtrsim 0.2T_c$ [see Fig. 16(a)], but in contrast to the symmetric case [see Fig. 12] the geometric phase at which the maximum is reached for $T \approx 0.2T_c$ is between successive multiples of $\pi/2$. Furthermore, it follows that the two solutions of Eq. (66) converge to one for $T \rightarrow 0.2T_c$. This effect can be understood in terms of Eq. (65), which is a cubic polynomial in $\sin(\Delta\varphi)$. Its discriminant is zero when Eq. (68) holds. In the present case, $|A| \ll |C|$, such that this condition reads $|B| = 4|C|/\sqrt{27} \approx 0.77|C|$. The value of $\Delta\varphi$ where this condition is met is given by Eq. (69), which for $|A| \ll |C|$ is approximately at $0.2\pi + k\pi$ and $0.8\pi + k\pi$. Our Fourier analysis confirms that this condition is met at $T \approx 0.22T_c$. Therefore, two solutions disappear when the temperature increases beyond this

threshold. As can be seen in Fig. 16(a), for temperatures near this threshold, there are extended ranges in $\Delta\varphi$ for which the spin diode efficiency is close to 100%. Fig. 16(b), which is for $T = 0.1T_c$, shows that varying the exchange field a change in the number of $\Delta\varphi$ values with perfect efficiency takes place around $J \approx 0.27E_F$. At $J = 0.4E_F$, corresponding to panel (a), solutions near $\Delta\varphi = (k + \frac{1}{2})\pi$ are present, whereas for $J = 0.1E_F$ these are absent. From our discussion of Eq. (67) the condition $|B| > 2|A|$ must be met for perfect efficiency around $\Delta\varphi = (k + \frac{1}{2})\pi$, and as the ratio $|B|/2|A|$ increases with J/E_F (it approaches zero for $J \rightarrow 0$), there is a critical $J/E_F \approx 0.27$ which must be exceeded for these solutions to exist. In Fig. 16(b) this is clearly visible.

2. Spontaneous Currents

Beside the diode efficiencies an interesting effect present in a SC/sFM/SC trilayer is the spontaneous current which is induced by the geometric phase difference $\Delta\varphi$. We concentrate on the spontaneous currents in asymmetric junctions because in this case the spontaneous spin current can be dominated by a second harmonic contribution. In our calculations, the barrier widths are spin-degenerate but mutually different: the left barrier has high transparency, $d_L = 0.6\lambda_F/2\pi$, and the right barrier is much less transparent, $d_R = 4.16\lambda_F/2\pi$.

In Fig. 17 we present the spontaneous charge [panel (a)] and spin [panel (b)] currents as functions of the temperature T and the geometric phase difference $\Delta\varphi$. The spontaneous charge current is well-approximated by

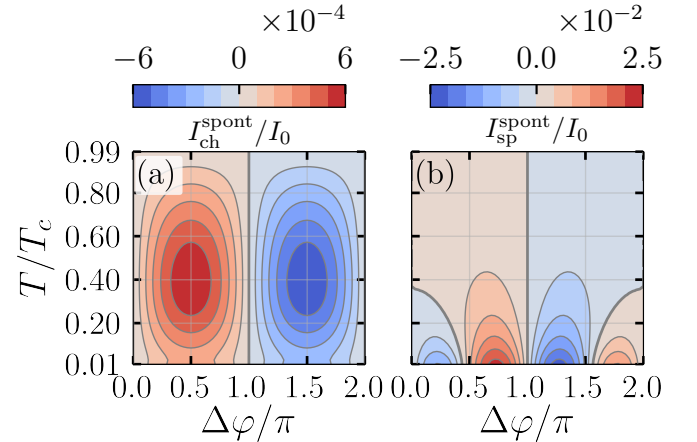


FIG. 17. Spontaneous charge [panel (a)] and spin [panel (b)] currents $I_{\text{ch/sp}}^{\text{spont}}$ as functions of geometric phase difference $\Delta\varphi$ and temperature T for an asymmetric junction with barrier potentials of height $V_B^{\uparrow} = 1.1E_F$ and $V_B^{\downarrow} = 1.7E_F$ and the band bottom in the sFM at $V_{\text{sFM}}^{\uparrow(\downarrow)} = \mp 0.3E_F$. The barrier widths are spin-degenerate with $d_L = 0.6\lambda_F/2\pi$ at the left barrier and $d_R = 4.16\lambda_F/2\pi$ at the right barrier.

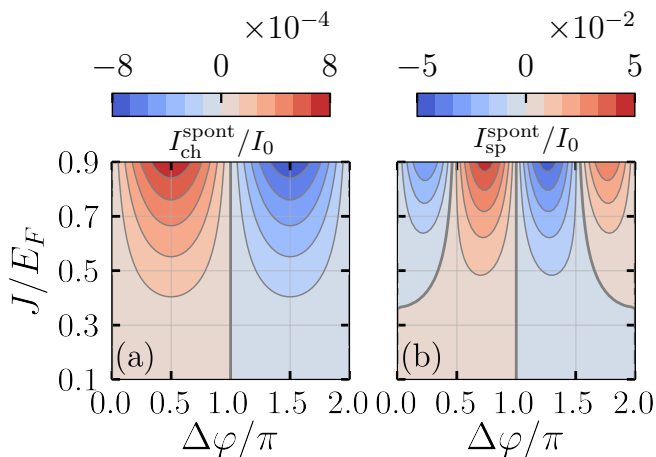


FIG. 18. Spontaneous charge [panel (a)] and spin [panel (b)] currents $I_{\text{ch/sp}}^{\text{spont}}$ as a function of the geometric phase difference and the exchange field strength J which is assumed to be the same in the barrier and the sFM, i.e. as in Fig. 13. The barrier widths are as for Fig. 17, i.e., for an asymmetric junction, and the temperature is $T = 0.1T_c$.

$I_{\text{ch}}(\Delta\chi = 0, \Delta\varphi, T) \approx I_{\text{ch}}^{(0)}(T) \sin(\Delta\varphi)$ where $I_{\text{ch}}^{(0)}(T)$ is maximum for $T \approx 0.4T_c$ and decreases for smaller or higher temperatures. In contrast, the spontaneous spin current shows a strong second harmonic at low temperatures which decreases with increasing temperatures. With T approaching T_c , it becomes purely sinusoidal.

Fig. 18 shows the spontaneous charge [panel (a)] and spin [panel (b)] currents as functions of the exchange field J and the geometric phase difference $\Delta\varphi$ for fixed temperature to $T = 0.1T_c$. The exchange field is assumed to have the same magnitude in the barriers and in the sFM. Similarly to the case discussed above, the spontaneous charge current is approximately sinusoidal as function of $\Delta\varphi$, with the pre-factor $I_{\text{ch}}^{(0)}(J)$ a monotonically increasing function of J . In contrast, the spontaneous spin current is strongly affected by J . For small J it is approximately sinusoidal in $\Delta\varphi$, whereas a second harmonic appears and becomes pronounced as the exchange field increases.

Appendix D: Density of states

The knowledge of the quasiclassical Green's function is sufficient to express most of relevant physical quantities. In particular, it allows calculating the spectral properties such as the local density of states (LDOS) besides the

transport properties. Having obtained the quasiclassical Green's function, the LDOS per spin projection, $N(z, E)$, is calculated via [80]

$$N_{\eta}(z, E) = N_{F\eta} \text{Re}[\mathcal{G}_{\eta\eta}(z, E)], \quad (\text{D1})$$

$$N(z, E) = \frac{1}{2} [N_{\uparrow}(z, E) + N_{\downarrow}(z, E)], \quad (\text{D2})$$

where $N_{F\eta}$ is the spin-resolved density of states at the Fermi level in the normal state.

In Fig. 19 we show the self-consistently obtained LDOS as a function of energy for (a) the symmetric junction considered in Fig. 5 and (b) the asymmetric junction considered in Fig. 6. In both panels, the solid lines correspond to the LDOS in the middle of the sFM and the dashed ones to the LDOS on the superconducting side of the right interface, i.e., sFM/SC interface. The zero-energy peaks visible in the solid lines in both panels is a result of the spin-triplet nature of the pair amplitudes in the sFM, which in the diffusive limit are all three odd-frequency correlations [2, 7, 114–117]. Instead of a mini-gap, expected in a conventional Josephson junction with a normal metal between two superconductors, here an enhanced density of states is observed near zero bias. The LDOS in the superconductor displays the coherence peaks close to the superconducting gap but still being far from the BCS density of states: the gap is either partly filled in the symmetric junction [panel (a)] or reduced in the asymmetric one [panel (b)]. For both junction types we recover the BCS density of states deep in the superconductors, i.e., close to the outer interfaces.

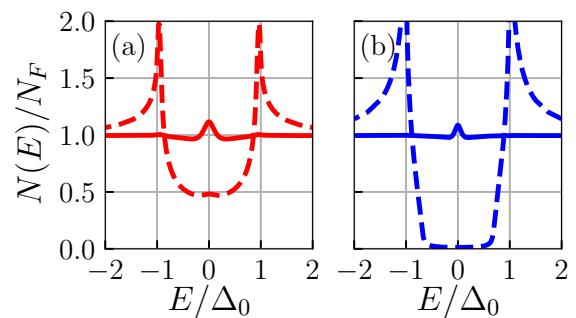


FIG. 19. Local density of states $N(E)$ (a) of the symmetric junction and (b) of the asymmetric junction. The solid lines show the LDOS in the center of the sFM, i.e., $z = 5.5\xi$ and the dashed lines the LDOS at the superconducting side of the right barrier, i.e., $z = 6\xi$. The superconducting and geometric phase difference are set to zero. The parameters of the symmetric and asymmetric case are the same as for Figs. 5 and 6, respectively.

[1] A. I. Buzdin, Proximity effects in superconductor-ferromagnet heterostructures, Rev. Mod. Phys. **77**, 935 (2005).

[2] F. S. Bergeret, A. F. Volkov, and K. B. Efetov, Odd triplet superconductivity and related phenomena in superconductor-ferromagnet structures, Rev. Mod.

- Phys. **77**, 1321 (2005).
- [3] M. Eschrig, T. Löfwander, T. Champel, J. C. Cuevas, J. Kopu, and G. Schön, Symmetries of Pairing Correlations in Superconductor–Ferromagnet Nanostructures, *J. Low Temp. Phys.* **147**, 457 (2007).
 - [4] M. Eschrig, Spin-polarized supercurrents for spintronics: A review of current progress, *Rep. Prog. Phys.* **78**, 104501 (2015).
 - [5] J. Linder and J. W. A. Robinson, Superconducting spintronics, *Nat. Phys.* **11**, 307 (2015).
 - [6] N. O. Birge, Spin-triplet supercurrents in Josephson junctions containing strong ferromagnetic materials, *Phil. Trans. R. Soc. A.* **376**, 20150150 (2018).
 - [7] J. Linder and A. V. Balatsky, Odd-frequency superconductivity, *Rev. Mod. Phys.* **91**, 045005 (2019).
 - [8] G. Yang, C. Ciccarelli, and J. W. A. Robinson, Boosting spintronics with superconductivity, *APL Materials* **9**, 050703 (2021).
 - [9] R. Cai, I. Žutić, and W. Han, Superconductor/ Ferromagnet Heterostructures: A Platform for Superconducting Spintronics and Quantum Computation, *Adv. Quantum Technol.* **6**, 2200080 (2023).
 - [10] M. Eschrig, J. Kopu, J. C. Cuevas, and G. Schön, Theory of Half-Metal/Superconductor Heterostructures, *Phys. Rev. Lett.* **90**, 137003 (2003).
 - [11] M. Eschrig and T. Löfwander, Triplet supercurrents in clean and disordered half-metallic ferromagnets, *Nat. Phys.* **4**, 138 (2008).
 - [12] R. Grein, M. Eschrig, G. Metalidis, and G. Schön, Spin-Dependent Cooper Pair Phase and Pure Spin Supercurrents in Strongly Polarized Ferromagnets, *Phys. Rev. Lett.* **102**, 227005 (2009).
 - [13] M. Eschrig, Scattering problem in nonequilibrium quasiclassical theory of metals and superconductors: General boundary conditions and applications, *Phys. Rev. B* **80**, 134511 (2009).
 - [14] R. Grein, T. Löfwander, and M. Eschrig, Inverse proximity effect and influence of disorder on triplet supercurrents in strongly spin-polarized ferromagnets, *Phys. Rev. B* **88**, 054502 (2013).
 - [15] M. Houzet and J. S. Meyer, Quasiclassical theory of disordered Rashba superconductors, *Phys. Rev. B* **92**, 014509 (2015).
 - [16] I. V. Bobkova, A. M. Bobkov, and M. A. Silaev, Gauge theory of the long-range proximity effect and spontaneous currents in superconducting heterostructures with strong ferromagnets, *Phys. Rev. B* **96**, 094506 (2017).
 - [17] J. A. Ouassou, A. Pal, M. Blamire, M. Eschrig, and J. Linder, Triplet Cooper pairs induced in diffusive s-wave superconductors interfaced with strongly spin-polarized magnetic insulators or half-metallic ferromagnets, *Sci. Rep.* **7**, 1932 (2017).
 - [18] M. Eschrig, Theory of Andreev bound states in S-F-S junctions and S-F proximity devices, *Phil. Trans. R. Soc. A* **376**, 20150149 (2018).
 - [19] F. S. Bergeret, A. F. Volkov, and K. B. Efetov, Long-Range Proximity Effects in Superconductor-Ferromagnet Structures, *Phys. Rev. Lett.* **86**, 4096 (2001).
 - [20] M. Eschrig, Spin-polarized supercurrents for spintronics, *Phys. Today* **64**, 43 (2011).
 - [21] R. S. Keizer, S. T. B. Goennenwein, T. M. Klapwijk, G. Miao, G. Xiao, and A. Gupta, A spin triplet supercurrent through the half-metallic ferromagnet CrO₂, *Nature* **439**, 825 (2006).
 - [22] T. S. Khaire, M. A. Khasawneh, W. P. Pratt, and N. O. Birge, Observation of Spin-Triplet Superconductivity in Co-Based Josephson Junctions, *Phys. Rev. Lett.* **104**, 137002 (2010).
 - [23] M. S. Anwar, F. Czeschka, M. Hesselberth, M. Porcu, and J. Aarts, Long-range supercurrents through half-metallic ferromagnetic CrO₂, *Phys. Rev. B* **82**, 100501 (2010).
 - [24] J. W. A. Robinson, J. D. S. Witt, and M. G. Blamire, Controlled Injection of Spin-Triplet Supercurrents into a Strong Ferromagnet, *Science* **329**, 59 (2010).
 - [25] J. W. A. Robinson, Gábor B. Halász, A. I. Buzdin, and M. G. Blamire, Enhanced Supercurrents in Josephson Junctions Containing Nonparallel Ferromagnetic Domains, *Phys. Rev. Lett.* **104**, 207001 (2010).
 - [26] J. Wang, M. Singh, M. Tian, N. Kumar, B. Liu, C. Shi, J. K. Jain, N. Samarth, T. E. Mallouk, and M. H. W. Chan, Interplay between superconductivity and ferromagnetism in crystalline nanowires, *Nat. Phys.* **6**, 389 (2010).
 - [27] J. Y. Gu, J. Kusunadi, and C.-Y. You, Proximity effect in a superconductor/exchange-spring-magnet hybrid system, *Phys. Rev. B* **81**, 214435 (2010).
 - [28] D. Sprungmann, K. Westerholt, H. Zabel, M. Weides, and H. Kohlstedt, Evidence for triplet superconductivity in Josephson junctions with barriers of the ferromagnetic Heusler alloy Cu₂MnAl, *Phys. Rev. B* **82**, 060505 (2010).
 - [29] L. Šmejkal, J. Sinova, and T. Jungwirth, Beyond conventional ferromagnetism and antiferromagnetism: A phase with nonrelativistic spin and crystal rotation symmetry, *Phys. Rev. X* **12**, 031042 (2022).
 - [30] Z. Feng, X. Zhou, L. Šmejkal, L. Wu, Z. Zhu, H. Guo, R. Gonzalez-Hernandez, X. Wang, H. Yan, P. Qin, X. Zhang, H. Wu, H. Chen, Z. Meng, L. Liu, Z. Xia, J. Sinova, T. Jungwirth, and Z. Liu, An anomalous Hall effect in altermagnetic ruthenium dioxide, *Nat. Electron.* **5**, 735 (2022).
 - [31] L. Šmejkal, J. Sinova, and T. Jungwirth, Emerging research landscape of altermagnetism, *Phys. Rev. X* **12**, 040501 (2022).
 - [32] C. L. Kane and E. J. Mele, Quantum Spin Hall Effect in Graphene, *Phys. Rev. Lett.* **95**, 226801 (2005).
 - [33] B. A. Bernevig, T. L. Hughes, and S.-C. Zhang, Quantum Spin Hall Effect and Topological Phase Transition in HgTe Quantum Wells, *Science* **314**, 1757 (2006).
 - [34] D. Hsieh, D. Qian, L. Wray, Y. Xia, Y. S. Hor, R. J. Cava, and M. Z. Hasan, A topological Dirac insulator in a quantum spin Hall phase, *Nature* **452**, 970 (2008).
 - [35] M. Z. Hasan, Colloquium: Topological insulators, *Rev. Mod. Phys.* **82**, 3045 (2010).
 - [36] Y. Ando, Topological Insulator Materials, *J. Phys. Soc. Jpn.* **82**, 102001 (2013).
 - [37] A. Bogdanov and A. Hubert, Thermodynamically stable magnetic vortex states in magnetic crystals, *J. Magn. Mater.* **138**, 255 (1994).
 - [38] U. K. Röbler, A. N. Bogdanov, and C. Pfleiderer, Spontaneous skyrmion ground states in magnetic metals, *Nature* **442**, 797 (2006).
 - [39] S. Mühlbauer, B. Binz, F. Jonietz, C. Pfleiderer, A. Rosch, A. Neubauer, R. Georgii, and P. Böni, Skyrmion Lattice in a Chiral Magnet, *Science* **323**, 915 (2009).
 - [40] X. Z. Yu, Y. Onose, N. Kanazawa, J. H. Park, J. H. Han,

- Y. Matsui, N. Nagaosa, and Y. Tokura, Real-space observation of a two-dimensional skyrmion crystal, *Nature* **465**, 901 (2010).
- [41] A. Fert, N. Reyren, and V. Cros, Magnetic skyrmions: advances in physics and potential applications, *Nat. Rev. Mater.* **2**, 17031 (2017).
- [42] A. A. Golubov, M. Yu. Kupriyanov, and E. Il'ichev, The current-phase relation in Josephson junctions, *Rev. Mod. Phys.* **76**, 411 (2004).
- [43] A. Buzdin, Direct Coupling Between Magnetism and Superconducting Current in the Josephson φ_0 Junction, *Phys. Rev. Lett.* **101**, 107005 (2008).
- [44] V. B. Geshkenbein and A. I. Larkin, The Josephson effect in superconductors with heavy fermions, *Pis'ma Zh. Eksp. Teor. Fiz.* **43**, 306 (1986) [*JETP Lett.* **43**, 395 (1986)].
- [45] S. Yip, Josephson current-phase relationships with unconventional superconductors, *Phys. Rev. B* **52**, 3087 (1995).
- [46] M. Sigrist, Time-reversal symmetry breaking states in high-temperature superconductors, *Prog. Theor. Phys.* **99**, 899 (1998).
- [47] M. Nadeem, M. S. Fuhrer, and X. Wang, The superconducting diode effect, *Nat. Rev. Phys.* **5**, 558 (2023).
- [48] F. Ando, Y. Miyasaka, T. Li, J. Ishizuka, T. Arakawa, Y. Shiotani, T. Moriyama, Y. Yanase, and T. Ono, Observation of superconducting diode effect, *Nature* **584**, 373 (2020).
- [49] C. Baumgartner, L. Fuchs, A. Costa, S. Reinhardt, S. Gronin, G. C. Gardner, T. Lindemann, M. J. Manfra, P. E. Faria Junior, D. Kochan, J. Fabian, N. Paradiso, and C. Strunk, Supercurrent rectification and magnetochiral effects in symmetric Josephson junctions, *Nat. Nanotechnol.* **17**, 39 (2022).
- [50] A. Costa, C. Baumgartner, S. Reinhardt, J. Berger, S. Gronin, G. C. Gardner, T. Lindemann, M. J. Manfra, J. Fabian, D. Kochan, N. Paradiso, and C. Strunk, Sign reversal of the Josephson inductance magnetochiral anisotropy and $0-\pi$ -like transitions in supercurrent diodes, *Nat. Nanotechnol.* **18**, 1266 (2023).
- [51] A. Gutfreund, H. Matsuki, V. Plastovets, A. Noah, L. Gorzawski, N. Fridman, G. Yang, A. Buzdin, O. Millo, J. W. A. Robinson, and Y. Anahory, Direct observation of a superconducting vortex diode, *Nat. Commun.* **14**, 1630 (2023).
- [52] Y. Hou, F. Nichele, H. Chi, A. Lodesani, Y. Wu, M. F. Ritter, D. Z. Haxell, M. Davydova, S. Ilić, O. Glezakou-Elbert, A. Varambally, F. S. Bergeret, A. Kamra, L. Fu, P. A. Lee, and J. S. Moodera, Ubiquitous Superconducting Diode Effect in Superconductor Thin Films, *Phys. Rev. Lett.* **131**, 027001 (2023).
- [53] E. Strambini, M. Spies, N. Ligato, S. Ilić, M. Rouco, C. Gonzalez-Orellana, M. Ilyn, C. Rogero, F. S. Bergeret, J. S. Moodera, P. Virtanen, T. T. Heikkilä, and F. Giazotto, Superconducting spintronic tunnel diode, *Nat. Commun.* **13**, 2431 (2022).
- [54] M. Trahms, L. Melischek, J. F. Steiner, B. Mahendru, I. Tamir, N. Bogdanoff, O. Peters, G. Reecht, C. B. Winkelmann, F. von Oppen, and K. J. Franke, Diode effect in Josephson junctions with a single magnetic atom, *Nature* **615**, 628 (2023).
- [55] A. Daido, Y. Ikeda, and Y. Yanase, Intrinsic Superconducting Diode Effect, *Phys. Rev. Lett.* **128**, 037001 (2022).
- [56] Ya. V. Fominov and D. S. Mikhailov, Asymmetric higher-harmonic SQUID as a Josephson diode, *Phys. Rev. B* **106**, 134514 (2022).
- [57] K. Halterman, M. Alidoust, R. Smith, and S. Starr, Supercurrent diode effect, spin torques, and robust zero-energy peak in planar half-metallic trilayers, *Phys. Rev. B* **105**, 104508 (2022).
- [58] J. J. He, Y. Tanaka, and N. Nagaosa, A phenomenological theory of superconductor diodes, *New J. Phys.* **24**, 053014 (2022).
- [59] S. Ilić and F. S. Bergeret, Theory of the Supercurrent Diode Effect in Rashba Superconductors with Arbitrary Disorder, *Phys. Rev. Lett.* **128**, 177001 (2022).
- [60] T. Karabassov, I. V. Bobkova, A. A. Golubov, and A. S. Vasenko, Hybrid helical state and superconducting diode effect in superconductor/ferromagnet/topological insulator heterostructures, *Phys. Rev. B* **106**, 224509 (2022).
- [61] A. A. Kopasov, A. G. Kutlin, and A. S. Mel'nikov, Geometry controlled superconducting diode and anomalous Josephson effect triggered by the topological phase transition in curved proximitized nanowires, *Phys. Rev. B* **103**, 144520 (2021).
- [62] K. Misaki and N. Nagaosa, Theory of the nonreciprocal Josephson effect, *Phys. Rev. B* **103**, 245302 (2021).
- [63] Y. Tanaka, B. Lu, and N. Nagaosa, Theory of giant diode effect in d-wave superconductor junctions on the surface of a topological insulator, *Phys. Rev. B* **106**, 214524 (2022).
- [64] N. F. Q. Yuan and L. Fu, Supercurrent diode effect and finite-momentum superconductors, *Proc. Natl. Acad. Sci.* **119**, e2119548119 (2022).
- [65] Y. Zhang, Y. Gu, P. Li, J. Hu, and K. Jiang, General Theory of Josephson Diodes, *Phys. Rev. X* **12**, 041013 (2022).
- [66] B. Zinkl, K. Hamamoto, and M. Sigrist, Symmetry conditions for the superconducting diode effect in chiral superconductors, *Phys. Rev. Res.* **4**, 033167 (2022).
- [67] R. S. Souto, M. Leijnse, and C. Schrade, Josephson Diode Effect in Supercurrent Interferometers, *Phys. Rev. Lett.* **129**, 267702 (2022).
- [68] J. F. Steiner, L. Melischek, M. Trahms, K. J. Franke, and F. Von Oppen, Diode Effects in Current-Biased Josephson Junctions, *Phys. Rev. Lett.* **130**, 177002 (2023).
- [69] A. Costa, J. Fabian, and D. Kochan, Microscopic study of the Josephson supercurrent diode effect in Josephson junctions based on two-dimensional electron gas, *Phys. Rev. B* **108**, 054522 (2023).
- [70] A. A. Kopasov, Zh. Devizorova, H. Meng, S. V. Mironov, A. S. Mel'nikov, and A. I. Buzdin, Adiabatic phase pumping in S/F/S hybrids with noncoplanar magnetization, *Phys. Rev. B* **108**, 224511 (2023).
- [71] R. Seoane Souto, M. Leijnse, C. Schrade, M. Valentini, G. Katsaros, and J. Danon, Tuning the Josephson diode response with an ac current, *Phys. Rev. Res.* **6**, L022002 (2024).
- [72] J. S. Meyer and M. Houzet, Josephson diode effect in a ballistic single-channel nanowire, *Appl. Phys. Lett.* **125**, 022603 (2024).
- [73] S. Ilić, P. Virtanen, D. Crawford, T. T. Heikkilä, and F. S. Bergeret, Superconducting diode effect in diffusive superconductors and Josephson junctions with Rashba spin-orbit coupling, *Phys. Rev. B* **110**, L140501 (2024).

- [74] A. V. Putilov, S. V. Mironov, and A. I. Buzdin, Nonreciprocal electron transport in finite-size superconductor/ferromagnet bilayers with strong spin-orbit coupling, *Phys. Rev. B* **109**, 014510 (2024).
- [75] J. B. Tjernshaugen, M. Amundsen, and J. Linder, Superconducting phase diagram and spin diode effect via spin accumulation, *Phys. Rev. B* **109**, 094516 (2024).
- [76] S. Patil, G. Tang, and W. Belzig, The Andreev-Ising-Josephson Diode, arXiv:2411.04061 [cond-mat.mes-hall] (2024).
- [77] G. D. Eilenberger, Transformation of Gorkov's equation for type II superconductors into transport-like equations, *Z. Phys.* **214**, 195 (1968).
- [78] A. I. Larkin and Y. N. Ovchinnikov, Quasiclassical Method in the Theory of Superconductivity, *Zh. Eksp. Teor. Fiz.* **55**, 2262 (1968) [*Sov. Phys. JETP* **28**, 1200 (1969)].
- [79] K. D. Usadel, Generalized Diffusion Equation for Superconducting Alloys, *Phys. Rev. Lett.* **25**, 507 (1970).
- [80] W. Belzig, F. K. Wilhelm, C. Bruder, G. Schön, and A. D. Zaikin, Quasiclassical Green's function approach to mesoscopic superconductivity, *Superlattices Microstruct.* **25**, 1251 (1999).
- [81] J. A. Sauls, Theory of disordered superconductors with applications to nonlinear current response, *Prog. Theor. Exp. Phys.* **2022**, 033103 (2022).
- [82] J. W. Serene and D. Rainer, The quasiclassical approach to superfluid ^3He , *Phys. Rep.* **101**, 221 (1983).
- [83] M. Eschrig, Distribution functions in nonequilibrium theory of superconductivity and Andreev spectroscopy in unconventional superconductors, *Phys. Rev. B* **61**, 9061 (2000).
- [84] N. Schopohl and K. Maki, Quasiparticle spectrum around a vortex line in a d-wave superconductor, *Phys. Rev. B* **52**, 490 (1995).
- [85] N. Schopohl, Transformation of the Eilenberger Equations of Superconductivity to a Scalar Riccati Equation, arXiv:cond-mat/9804064 [cond-mat.supr-con] (1998).
- [86] Y. Nagato, K. Nagai, and J. Hara, Theory of the Andreev reflection and the density of states in proximity contact normal-superconducting infinite double-layer, *J. Low Temp. Phys.* **93**, 33 (1993).
- [87] S. Higashitani and K. Nagai, Meissner Effect in Normal-Superconducting Proximity-Contact Double Layers, *J. Phys. Soc. Jpn.* **64**, 549 (1995).
- [88] M. Eschrig, J. A. Sauls, and D. Rainer, Electromagnetic response of a vortex in layered superconductors, *Phys. Rev. B* **60**, 10447 (1999).
- [89] M. Eschrig, J. Kopu, A. Konstandin, J. Cuevas, M. Fogelström, and G. Schön, Singlet-Triplet Mixing in Superconductor-Ferromagnet Hybrid Devices, in *Advances in Solid State Physics*, edited by B. Kramer (Springer Berlin Heidelberg, Berlin, Heidelberg, 2004) pp. 533–545.
- [90] A. Konstandin, J. Kopu, and M. Eschrig, Superconducting proximity effect through a magnetic domain wall, *Phys. Rev. B* **72**, 140501(R) (2005).
- [91] J. C. Cuevas, J. Hammer, J. Kopu, J. K. Viljas, and M. Eschrig, Proximity effect and multiple Andreev reflections in diffusive superconductor-normal-metal-superconductor junctions, *Phys. Rev. B* **73**, 184505 (2006).
- [92] M. Eschrig, A. Cottet, W. Belzig, and J. Linder, General boundary conditions for quasiclassical theory of superconductivity in the diffusive limit: Application to strongly spin-polarized systems, *New J. Phys.* **17**, 083037 (2015).
- [93] J. A. X. Alexander, T. P. Orlando, D. Rainer, and P. M. Tedrow, Theory of Fermi-liquid effects in high-field tunneling, *Phys. Rev. B* **31**, 5811 (1985).
- [94] T. Tokuyasu, J. A. Sauls, and D. Rainer, Proximity effect of a ferromagnetic insulator in contact with a superconductor, *Phys. Rev. B* **38**, 8823 (1988).
- [95] R. Fazio and C. Lucheroni, Local density of states in superconductor-ferromagnetic hybrid systems, *Europhys. Lett.* **45**, 707-713 (1999).
- [96] J. Gelhausen and M. Eschrig, Theory of a weak-link superconductor-ferromagnet Josephson structure, *Phys. Rev. B* **94**, 104502 (2016).
- [97] M. Fogelström, Josephson currents through spin-active interfaces, *Phys. Rev. B* **62**, 11812 (2000).
- [98] J. C. Cuevas and M. Fogelström, Quasiclassical description of transport through superconducting contacts, *Phys. Rev. B* **64**, 104502 (2001).
- [99] J. Kopu, M. Eschrig, J. C. Cuevas, and M. Fogelström, Transfer-matrix description of heterostructures involving superconductors and ferromagnets, *Phys. Rev. B* **69**, 094501 (2004).
- [100] E. Zhao, T. Löfwander, and J. A. Sauls, Nonequilibrium superconductivity near spin-active interfaces, *Phys. Rev. B* **70**, 134510 (2004).
- [101] C. J. Lambert, Generalized Landauer formulae for quasi-particle transport in disordered superconductors, *J. Phys. Condens. Matter* **3**, 6579 (1991).
- [102] C. W. J. Beenakker, Quantum transport semiconductor-superconductor microjunctions, *Phys. Rev. B* **46**, 12841 (1992).
- [103] Y. Takane and H. Ebisawa, Conductance of Normal-Superconductor Contacts Due to the Andreev Reflection, *J. Phys. Soc. Jpn.* **61**, 3466 (1992).
- [104] R. Grein, T. Löfwander, G. Metalidis, and M. Eschrig, Theory of superconductor-ferromagnet point-contact spectra: The case of strong spin polarization, *Phys. Rev. B* **81**, 094508 (2010).
- [105] E. V. Thuneberg, J. Kurkijarvi, and D. Rainer, Quasiclassical theory of ions in ^3He , *J. Phys. C: Solid State Phys.* **14**, 5615 (1981).
- [106] Y. V. Nazarov, Novel circuit theory of Andreev reflection, *Superlattices Microstruct.* **25**, 1221 (1999).
- [107] S. H. Jacobsen, J. A. Ouassou, and J. Linder, Critical temperature and tunneling spectroscopy of superconductor-ferromagnet hybrids with intrinsic Rashba-Dresselhaus spin-orbit coupling, *Phys. Rev. B* **92**, 024510 (2015).
- [108] A. L. Shelankov, On the derivation of quasiclassical equations for superconductors, *J. Low Temp. Phys.* **60**, 29 (1985).
- [109] M. Y. Kuprianov and V. F. Lukichev, Influence of boundary transparency on the critical current of "dirty" SS'S structures, *Zh. Eksp. Teor. Fiz.* **94**, 139 (1988) [*Sov. Phys. JETP* **67**, 1163 (1988)].
- [110] C. Sun and J. Linder, Gate-tunable sign reversal of dissipationless spin-diode effect reaching 100%, arXiv:2410.07337 [cond-mat.supr-con] (2024).
- [111] Y. Mao, Q. Yan, Y.-C. Zhuang, and Q.-F. Sun, Universal Spin Superconducting Diode Effect from Spin-Orbit Coupling, *Phys. Rev. Lett.* **132**, 216001 (2024).
- [112] M. Eschrig, Phase-sensitive Interface and Proximity

- Effects in Superconducting Spintronics, in *Spintronics Handbook, Second Edition: Spin Transport and Magnetism: Volume One: Metallic Spintronics*, edited by E. Tsymbal and I. Žutić (CRC Press, 2019) pp. 635–682.
- [113] A. Bauer, J. Bentner, M. Aprili, M. L. Della Rocca, M. Reinwald, W. Wegscheider, and C. Strunk, Spontaneous Supercurrent Induced by Ferromagnetic π Junctions, *Phys. Rev. B* **92**, 217001 (2004).
- [114] T. Yokoyama, Y. Tanaka, and A. A. Golubov, Resonant peak in the density of states in the normal metal/diffusive ferromagnet/superconductor junctions *Phys. Rev. B* **72**, 052512 (2005).
- [115] T. Yokoyama, Y. Tanaka, and A. A. Golubov, Manifestation of the odd-frequency spin-triplet pairing state in diffusive ferromagnet/superconductor junctions, *Phys. Rev. B* **75**, 134510 (2007).
- [116] Y. Tanaka and A. A. Golubov, Theory of the Proximity Effect in Junctions with Unconventional Superconductors, *Phys. Rev. Lett.* **98**, 037003 (2007).
- [117] A. Di Bernardo, S. Diesch, Y. Gu, J. Linder, G. Divitini, C. Ducati, E. Scheer, M. Blamire, and J. Robinson, Signature of magnetic-dependent gapless odd frequency states at superconductor/ferromagnet interfaces, *Nat. Commun.* **6**, 8053 (2015).